

# 1 Global structure of magnetotail reconnection revealed by mining 2 space magnetometer data

3 **G. K. Stephens<sup>1</sup>, M. I. Sitnov<sup>1</sup>, R. S. Weigel<sup>2</sup>, D. L. Turner<sup>1</sup>, N. A. Tsyganenko<sup>3</sup>, A. J.  
4 Rogers<sup>4</sup>, K. Genestreti<sup>5</sup>, and J. A. Slavin<sup>6</sup>**

5 <sup>1</sup>The Johns Hopkins University Applied Physics Laboratory, Laurel, MD 20723, USA

6 <sup>2</sup>George Mason University, Fairfax, VA 22030, USA

7 <sup>3</sup>Saint-Petersburg State University, Saint-Petersburg, Russia

8 <sup>4</sup>University of New Hampshire, Durham, NH, USA

9 <sup>5</sup>Space Science and Engineering, Southwest Research Institute, Durham, NH, USA

10 <sup>6</sup>Department of Climate and Space Sciences and Engineering, University of Michigan, Ann Arbor, MI, USA

## 11 **Key Points:**

- 12 • Global structure of magnetotail reconnection inferred from data mining matches its lo-  
13 cations revealed by in-situ observations
- 14 • Reconstructed magnetotail reconnection structures include X- and O-lines and magnetic  
15 nulls
- 16 • Reconstructed multiscale current sheet structure is consistent with its formation mech-  
17 anism by quasi-adiabatic ion motions

**Abstract**

Reconnection in the magnetotail occurs along so-called X-lines, where magnetic field lines tear and detach from plasma on microscopic spatial scales (comparable to particle gyroradii). In 2017–2020 the Magnetospheric MultiScale (MMS) mission detected X-lines in the magnetotail enabling their investigation on local scales. However, the global structure and evolution of these X-lines, critical for understanding their formation and total energy conversion mechanisms, remained virtually unknown because of the intrinsically local nature of observations and the extreme sparsity of concurrent data. Here we show that mining a multi-mission archive of space magnetometer data collected over the last 26 years and then fitting a magnetic field representation modeled using flexible basis-functions faithfully reconstructs the global pattern of X-lines; 24 of the 26 modeled X-lines match ( $B_z = 0$  isocontours are within  $\sim 2$  Earth radii or  $R_E$ ) or nearly match ( $B_z = 2$  nT isocontours are within  $\sim 2R_E$ ) the locations of the MMS encountered reconnection sites. The obtained global reconnection picture is considered in the context of substorm activity, including conventional substorms and more complex events.

**Plain Language Summary**

Magnetic reconnection is a fundamental process in plasmas which couples microscopic scales ( $\sim$ electron to proton gyroradii) to explosive macroscopic phenomena many orders of magnitude larger, such as solar flares and geomagnetic storms/substorms. Reconnection forms along “X-lines”, rifts where oppositely directed magnetic field lines are forced together. In the Earth’s magnetosphere, reconnection has been observed by satellites at isolated locations; however, the large-scale structure of X-lines and their time evolution remains unknown because of the rarity and local nature of observations. Here, ground based measurements of geomagnetic activity and solar wind measurements are used to data-mine 26 years of magnetometer data from 22 Earth-orbiting satellites, which are then utilized to reconstruct the global magnetic field associated with X-lines in Earth’s magnetosphere. We show that these reconstructions pinpoint the reconnection locations by verifying their consistency with direct spacecraft observations.

**1 Introduction**

X-lines are one of the most fundamental structures in magnetized plasmas, particularly in space, where they link global or even astronomical scale processes to those on the single particle orbit scale, thereby allowing those microscale processes to shape the universe (Ji et al., 2022). Dungey (1961) suggested that the interaction between Earth’s magnetic dipole and the solar wind causes reconnection of magnetic field lines on both the day and nightsides of Earth’s magnetosphere. The shape of these reconnecting field lines resembles the letter “X” and extends tens of Earth radii ( $R_E = 6,371.2$  kilometers) in the dawn-dusk direction thus forming X-lines. An X-line divides space into four sectors. In one pair of opposing sectors, the magnetic field and plasma converge towards the center of the X while in the other pair they are rapidly ejected from it. This reconnection process transforms energy stored in the magnetic field into particle kinetic and thermal energy, making it an efficient energy converter and particle accelerator (Ji et al., 2022). X-lines couple kinetic processes on proton and even electron gyroradius scales ( $\lesssim 0.01R_E$ ) (Torbert et al., 2018) to space weather phenomena on global scales: such as solar flares, coronal mass ejections, and magnetospheric storms and substorms ( $\sim 10R_E$ ) (Camporeale, 2019). This range of scales is so immense that its modeling has become one of the major challenges for nascent exascale computing (Ji et al., 2022).

While the microscale physics of reconnection in the magnetosphere has been studied in detail using recent multi-probe satellite missions (Angelopoulos et al., 2008; Burch, Moore, et al., 2016; Burch, Torbert, et al., 2016; Torbert et al., 2018), its global structure is difficult to infer from data due to their paucity (rarity and locality): at any moment the huge volume of the magnetosphere ( $\gtrsim 10^5 R_E^3$ ) is probed by less than a dozen spacecraft (Sitnov, Stephens, et al., 2019). Understanding the global structure of reconnection is fundamental for determining substorm triggering mechanisms (Sitnov, Birn, et al., 2019) and the total energy conversion during storms and

68 substorms (Angelopoulos et al., 2013; Angelopoulos et al., 2020). Further, if X-line maps can  
 69 be constructed from data, these maps could guide large-scale magnetohydrodynamic simulations  
 70 of the magnetosphere by introducing a non-zero resistivity at their locations (Birn et al., 1996).

71 On the dayside, the X-line location can be readily estimated from the global geometry of  
 72 the solar wind and Earth's magnetic fields along with other well-defined physical parameters (Fuselier  
 73 et al., 2011). In contrast, nightside reconnection is much less understood. Here, the solar wind-  
 74 magnetosphere interaction stretches the dipole field lines in the antisunward direction forming  
 75 the magnetotail while storing energy in the magnetic field. The release of this stored energy via  
 76 reconnection is often unsteady and spontaneous. Observations of substorms (McPherron et al.,  
 77 1973; Russell & McPherron, 1973; Hones Jr., 1984; Baker et al., 1996; Angelopoulos et al., 2008,  
 78 2013) suggest that new X-lines form in the tail at distances of  $10\text{--}30R_E$  and that this distance is  
 79 controlled by the solar wind input (Nagai et al., 2005; Nagai & Shinohara, 2022). However, de-  
 80 spite decades of debate and being the target of dedicated satellite missions (Nagai et al., 2005;  
 81 Angelopoulos et al., 2008; Burch, Moore, et al., 2016), the factors that determine the emergence,  
 82 location, size, and shape of nightside X-lines remain a major mystery in heliophysics.

83 The recent four-probe Magnetospheric MultiScale (MMS) mission (Burch, Moore, et al.,  
 84 2016) enabled microscopic analysis of magnetotail reconnection down to electron gyroradius scales (Torbert  
 85 et al., 2018). During four years of MMS observations, 26 potential X-line encounters were found  
 86 in the magnetotail (Rogers et al., 2019, 2021), where explosive reconnection causes substorms  
 87 (Angelopoulos et al., 2008; Angelopoulos et al., 2020; Sitnov, Stephens, et al., 2019). They were  
 88 detected in the form of Ion Diffusion Regions (IDRs) characterized by reversals of the North-  
 89 South component of the magnetic field,  $B_z$ , and of the Sun-Earth component of the proton bulk  
 90 flow velocity,  $v_x$ .

91 In this study, the global structure of magnetotail reconnection is derived from a large set  
 92 of historic satellite magnetometer measurements using an advanced data mining (DM) approach  
 93 combined with a flexible analytical model of the magnetospheric current systems. We show that  
 94 our technique provides evidence justifying the global reconnection structure: the obtained con-  
 95 tours delineating  $B_z$  reversals pass through most of the micro-scale IDRs observed by MMS (sec-  
 96 tion 3). We further discuss implications of the obtained magnetotail picture to the multiscale struc-  
 97 ture of its current sheet (section 3.2), and then describe its uncertainty and in-situ validation er-  
 98 rors (section 4). We then discuss the global X-line structure in the context of substorm activity  
 99 (section 5). This includes the evolution of the magnetotail structure during a particular substorm  
 100 event and some unusual substorm effects. The results are summarized in section 6. Throughout  
 101 this study, vector quantities are represented in the Geocentric Solar Magnetospheric System (GSM).

## 102 2 Data Mining Solution of the Data Paucity Problem

103 The key to solving the data paucity problem lies in the recurrent nature and repeatable pat-  
 104 tern of storms and substorms. The storm recurrence time for medium intensity storms is approx-  
 105 imately two weeks (Reyes et al., 2021), while it is 2–4 h for periodic substorm (Borovsky & Yaky-  
 106 menko, 2017). This repeatability allows the magnetic field to be reconstructed not only from ob-  
 107 servations at the moment of interest but also from records identified via mining the space mag-  
 108 netometer archive (section 2.1) by searching for other times when the magnetosphere was in a  
 109 similar global state. The magnetospheric state is characterized using geomagnetic indices (met-  
 110 rics of magnetic activity derived from networks of ground magnetometers) and solar wind con-  
 111 ditions. Specifically, the magnetospheric state is defined using a 5D state-space vector,  $\mathbf{G}(t) =$   
 112  $(G_1, \dots, G_5)$ , formed from the geomagnetic storm index (*SMR*), substorm index (*SML*), their time  
 113 derivatives, and the solar wind electric field parameter ( $vB_z^{IMF}$ ; where  $v$  is the solar wind speed  
 114 and  $B_z^{IMF}$  is the North-South component of the Interplanetary Magnetic Field, IMF). The *SMR*  
 115 and *SML* (*SMR* is a pressure-corrected *SMR* (Tsyganenko, Andreeva, Sitnov, et al., 2021)) in-  
 116 dices are provided by the SuperMag project (Gjerloev, 2012) and represent variations of the ground-  
 117 based magnetometer records from low/mid- and high-latitude stations respectively analogous to

118 the *Sym-H* and *AL* indices used before (Sitnov et al., 2008; Stephens et al., 2019). Further details  
119 on the magnetospheric state-space are provided in section 2.2.

120 The DM algorithm employed is based on the k-nearest neighbor (kNN) classifier method  
121 (Wettschereck et al., 1997; Sitnov et al., 2008). To illustrate the algorithm, assume the magnetic  
122 field reconstruction,  $\mathbf{B}(t)$ , is sought for a query time  $t = t^{(q)}$ . This corresponds to a particular point  
123 in the 5D state-space,  $\mathbf{G}^{(q)} = \mathbf{G}(t^{(q)})$ . Surrounding this point will be other points,  $\mathbf{G}^{(i)}$ , in close  
124 proximity to it; i.e., its nearest neighbors (NNs). Distances between points in state-space are com-  
125 puted using the Euclidean metric. These NNs identify a relatively small subset of data from a large  
126 magnetometer database that are then used to fit a magnetic field model, yielding  $\mathbf{B}(t^{(q)})$ . The spe-  
127 cific choice of the number of NNs to use in the reconstruction,  $k_{NN}$ , is dictated by a balance be-  
128 tween over- and under-fitting. Stephens and Sitnov (2021) found the optimal number to be  $k_{NN} =$   
129 32,000 for tail reconstructions of substorms, corresponding to  $\sim 1\%$  of the total database. The  
130 resulting subset is composed of a very small number ( $\sim 1\text{--}10$ ) of real (from the event of inter-  
131 est) but many ( $\sim 10^5$ ) virtual (from other events) satellites. See section 2.3 for a more detailed  
132 description.

133 The large number of virtual points enables new magnetic field architectures (Tsyganenko  
134 & Sitnov, 2007; Stephens et al., 2019), which differ from classical empirical models with custom-  
135 tailored modules (e.g., Tsyganenko & Sitnov, 2005) by utilizing regular basis function expan-  
136 sions for the major magnetospheric current systems, to be used for the reconstructions. In par-  
137 ticular, all near-equatorial currents are approximated by two expansions representing general cur-  
138 rent distributions of thick and thin current sheets with different thickness parameters  $D$  and  $D_{TCS}$ .  
139 The latter accounts for the formation of ion-scale thin current sheets (TCS) prior to substorm on-  
140 set (Sergeev et al., 2011) as is further discussed in section 2.4.

141 The solar wind plasma and IMF measurements were obtained from the NASA Space Physics  
142 Data Facility through OMNIWeb ([https://omniweb.gsfc.nasa.gov/ow\\_min.html](https://omniweb.gsfc.nasa.gov/ow_min.html)). OMNIWeb uti-  
143 lizes solar wind measurements from the ACE, Wind, IMP 8, and Geotail mission's magnetic field  
144 and plasma instruments applying a time delay to propagate them to the bow shock nose. The 5-  
145 min cadence OMNI products were used throughout this study, including the values for the so-  
146 lar wind velocity, flow pressure, and the IMF. The *SML* and *SMR* 1-min indices were downloaded  
147 from the SuperMAG webpage (<https://supermag.jhuapl.edu/indices>).

148 The methodology (DM algorithm and magnetic field architecture) presented here advances  
149 that of previous works, notably Stephens et al. (2019). The primary changes are: (i) an updated  
150 magnetometer archive, (ii) replacing the *Sym-H* and *AL* indices by *SMR* and *SML* respectively,  
151 (iii) distance-weighting of the NNs, (iv) new spatial dependent TCS module, and (v) the “bowl-  
152 shaped” deformation for the equatorial current sheet. The remainder of this section (2.1–2.4) pro-  
153 vides additional details on the above summary and is provided here for completeness.

## 154 2.1 Archive of Space Magnetometer Data

155 The heritage of the space magnetometer data used in this study dates to earlier empirical  
156 models of storms (Tsyganenko & Sitnov, 2007) and subsequent DM reconstructions (Sitnov et  
157 al., 2008). As the DM approach relies on knowledge of the solar wind plasma and IMF condi-  
158 tions, the start of the magnetometer archive (January 1995) was chosen to approximately coin-  
159 cide with the advent of continuous long-term L1 monitoring of the upstream solar wind which  
160 began in late 1994 with the launch of the Wind spacecraft. That archive (Tsyganenko & Sitnov,  
161 2007) consisted of magnetic field observations from the IMP-8, Geotail, the Geosynchronous GOES-  
162 8, 9, 10, and 12 satellites, Cluster, and Polar missions. The time-resolution of the magnetome-  
163 ter data provided by the missions is often higher than is necessary for global scale reconstruc-  
164 tions, so it is common practice to downsample the original data source to a regular cadence by  
165 time-averaging over multiple measurements (e.g., Tsyganenko, Andreeva, Kubyshkina, et al., 2021).  
166 A decision must then be made for the frequency of the downsampled data. The archive from Tsyganenko  
167 and Sitnov (2007) and Sitnov et al. (2008) choose 15 min averaging cadence except for when space-

168 craft were located within  $r < 5R_E$ , in which the higher spacecraft velocities prompted for a 5 min  
 169 data cadence. This archive is available at [http://geo.phys.spbu.ru/~tsyganenko/data\\_sets.html](http://geo.phys.spbu.ru/~tsyganenko/data_sets.html).

170 The data archive from Tsyganenko and Sitnov (2007) was later augmented for the DM reconstructions of substorms by updating the Polar and Cluster datasets and by adding the THEMIS  
 171 and Van Allen probes magnetometer data (Stephens et al., 2019). This expansion proved useful  
 172 in populating the equatorial inner magnetosphere and near-tail region with data. In constructing  
 173 this archive, the data from these four missions was averaged to a 5 min cadence, but when incor-  
 174 porated into the DM algorithm, it was downsampled to 15 min when the spacecraft location was  
 175  $r \geq 5R_E$  to be consistent with the earlier archive. This extended database (including the Tsyganenko  
 176 and Sitnov (2007) database) is available on the NASA Space Physics Data Facility: [https://spdf.gsfc.nasa.gov/pub/data/aaa\\_spepurpose-datasets/empirical-magnetic-field-modeling-database-with-TS07D-coefficients/](https://spdf.gsfc.nasa.gov/pub/data/aaa_spepurpose-datasets/empirical-magnetic-field-modeling-database-with-TS07D-coefficients/). This  
 177 archive was again extended in subsequent substorm reconstructions by adding the available MMS  
 178 data, which at that time had completed a full season sampling the midtail following the exten-  
 179 sion of the MMS apogee to  $r \approx 25R_E$  (Sitnov, Stephens, et al., 2019; Stephens & Sitnov, 2021).  
 180 The addition of MMS data proved useful in the reconstruction of the mid-tail region including  
 181 the resolution of X-line features (Sitnov, Stephens, et al., 2019). For those substorm reconstruc-  
 182 tions, data beyond the primary apogee of the Geotail mission,  $r = 31R_E$ , was filtered. This was  
 183 performed primarily to remove data points from the two THEMIS probes as they transitioned to  
 184 the ARTEMIS orbit, as the inclusion of this distant data could produce anomalous results (Stephens  
 185 et al., 2019).

186 In this study, the magnetometer data archive has again been updated. First, given the im-  
 187 portance of the MMS dataset to this particular investigation, it was extended through the end of  
 188 the year 2020, now encompassing three full tail seasons. Further, in February of 2019, the MMS  
 189 apogee was raised from  $r \approx 25R_E$  to  $r \approx 29R_E$  (Williams et al., 2020), increasing the amount  
 190 of data in this region. Second, the THEMIS, Cluster, Van Allen Probes, and MMS datasets were  
 191 all downsampled to a universal 5 min cadence, instead of switching between 5 and 15 min based  
 192 on spacecraft's radial distance. The motivation being that the previous substorm investigations  
 193 demonstrated that the DM approach can indeed reconstruct changes in the magnetosphere on the  
 194 scale approaching 5 min resolution (Stephens et al., 2019; Sitnov, Stephens, et al., 2019). The  
 195 remaining spacecraft datasets (Geotail, IMP-8, and GOES satellites) retain the 15 min data ca-  
 196 dence. The third is that the radial filter was increased from  $31R_E$  to  $36R_E$ . Although, as Figure S1  
 197 indicates, the data between  $31R_E$  and  $36R_E$  is relatively sparse, its inclusion was found to help  
 198 stabilize the reconstructions in the region  $r \approx 25\text{--}31R_E$ , which was of particular importance for  
 199 this study. The result is an archive of 8,649,672 magnetometer data records spanning the years  
 200 1995–2020 and radial distance 1.5 to  $36R_E$ . The resulting spatial distribution of the records is  
 201 shown in Figure S1 while the breakdown of each individual spacecraft's contribution to the archive  
 202 is displayed in Table 1.

203 The general process for constructing these datasets is as follows. First, the magnetometer  
 204 data is downloaded from either the mission webpage or a community resource such as the NASA  
 205 Space Physics Data Facility. Any anomalous data records are removed. The contribution of the  
 206 internal magnetic field is removed utilizing the International Geomagnetic Reference Field (IGRF)  
 207 model (Alken et al., 2021). Data collected when the spacecraft was outside the magnetopause  
 208 is filtered by either visual determination of magnetopause crossings or by application of em-  
 209 pirical magnetopause models (e.g., Shue et al., 1998). The resulting data are then downsampled  
 210 to the requisite data cadence using boxcar averaging. As one approaches the surface of the Earth,  
 211 the magnitude of the background magnetic field,  $|\mathbf{B}_{int}|$ , becomes very large relative to the mag-  
 212 netic field generated by external current sources,  $|\mathbf{B}_{ext}|$ . Thus, distinguishing the external and in-  
 213 ternal fields requires attitude knowledge beyond the capacity of many spacecraft missions. For  
 214 these reasons data is excluded when  $r < 1.5R_E$  for equatorial orbiting spacecraft. For polar or-  
 215 biting spacecraft (Polar and Cluster), a larger exclusion radius of  $r < 3.2R_E$  was used to prevent  
 216 the large magnetic field deviations due to low-altitude FACs from biasing the fit.

**Table 1.** The Archive of Space Magnetometer Data.

Spacecraft	Number	Period	Cadence (min)
Cluster 1	756,822	2001–2015	5
Cluster 2	753,580	2001–2015	5
Cluster 3	748,084	2001–2015	5
Cluster 4	561,497	2001–2015	5
Geotail	133,107	1995–2005	15
Polar	844,212	1996–2006	5
IMP-8	10,177	1995–2000	15
GOES-8	233,674	1995–2003	15
GOES-9	84,951	1995–1998	15
GOES-10	213,295	1999–2005	15
GOES-12	79,569	2003–2005	15
THEMIS-A	702,043	2008–2015	5
THEMIS-B	78,523	2008–2011	5
THEMIS-C	115,459	2008–2011	5
THEMIS-D	702,388	2008–2015	5
THEMIS-E	711,441	2008–2015	5
Van Allen A	337,582	2012–2016	5
Van Allen B	337,610	2012–2016	5
MMS 1	312,040	2015–2020	5
MMS 2	312,050	2015–2020	5
MMS 3	311,349	2015–2020	5
MMS 4	310,219	2015–2020	5
Total	8,649,672	1995–2020	5/15

## 2.2 Storm-Substorm-Solar Wind State-Space

219 Storms and substorms and their response to solar wind drivers have a tendency to develop  
 220 in repeatable and predictable ways as indicated by their manifestation in geomagnetic indices (e.g.,  
 221 Liemohn et al., 2018). This makes their empirical reconstruction using DM possible. To do this,  
 222 the storm/substorm state of the magnetosphere is assumed to be characterizable using a low-dimensional  
 223 state-space (Vassiliadis, 2006). For example, earlier storm studies formulated a 3D state-space  
 224 based on the storm-time index *Sym-H*, its time derivative, and the solar wind electric field param-  
 225 eter  $vB_z^{IMF}$  (Sitnov et al., 2008) (where  $v$  is the  $X$  component of the solar wind bulk velocity which  
 226 is multiplied by the  $Z$  component of the IMF in GSM coordinates), the idea being that these three  
 227 parameters are representative of the storm-state of the magnetosphere (Burton et al., 1975; Vas-  
 228 siliadis et al., 1999). At any given moment in time the storm-state of the magnetosphere is rep-  
 229 resented as a state-vector,  $\mathbf{G}(t)$ , within this state-space. As the storm develops, it will plot a tra-  
 230 jectory through this state-space and similar events will trace similar trajectories. Subsequent sub-  
 231 storm investigations expanded to a 5D state-space by adding the substorm index *AL* along with  
 232 its time derivative (Stephens et al., 2019). For this study, the *AL* and *Sym-H* indices have been  
 233 replaced by their SuperMAG counterparts (Gjerloev, 2012), *SML* and *SMR* respectively (Newell  
 234 & Gjerloev, 2011, 2012). The primary reason for this change was that, as of the writing of this  
 235 study, the digital values for the *AL* index are not available beyond March of 2018. This would  
 236 have nullified the expansion of the MMS dataset discussed in the previous section. Further, the  
 237 SuperMAG indices are computed using a much larger number of ground magnetometer stations  
 238 (on the order of  $\sim 100$  instead of  $\sim 10$  that are used for *AL* and *Sym-H*). In particular, the higher  
 239 density and smaller gaps between stations allows the *SML* index to detect substorms that may be  
 240 missed by the *AL* index (Newell & Gjerloev, 2011). As with the earlier studies, the storm index  
 241

242 has been pressure corrected to remove magnetic perturbations caused by the compression of the  
 243 magnetopause (Gonzalez et al., 1994). The pressure corrected index,  $SMRc$ , is defined:  $SMRc =$   
 244  $0.8 \cdot SMR - 13\sqrt{P_{dyn}}$  (Tsyganenko, Andreeva, Sitnov, et al., 2021). The 5D storm/substorm state-  
 245 space used here is defined:

$$G_1(t) = \langle SMRc | \propto \int_{-\Pi_{st}/2}^0 SMRc(t + \tau) \cos(\pi\tau/\Pi_{st}) d\tau \quad (1)$$

$$G_2(t) = D\langle SMRc | / Dt \propto \int_{-\Pi_{st}/2}^0 SMRc(t + \tau) \cos(2\pi\tau/\Pi_{st}) d\tau \quad (2)$$

$$G_3(t) = \langle SML | \propto \int_{-\Pi_{sst}/2}^0 SML(t + \tau) \cos(\pi\tau/\Pi_{sst}) d\tau \quad (3)$$

$$G_4(t) = D\langle SML | / Dt \propto \int_{-\Pi_{sst}/2}^0 SML(t + \tau) \cos(2\pi\tau/\Pi_{sst}) d\tau \quad (4)$$

$$G_5(t) = \langle vB_s^{IMF} | \propto \int_0^{\tau_\infty} vB_s^{IMF}(t - \tau_\infty + \tau) \exp[(\tau - \tau_\infty)/\tau_0] d\tau \quad (5)$$

246 The integration convolves the original time-series data with smoothing windows, indicated  
 247 by the  $\langle \dots |$  notation. In the case of eq. (1) and eq. (3) the windows are half cosines which acts  
 248 to smooth  $SMRc$  and  $SML$  over storm ( $\Pi_{st}/2 = 6$  h) and substorms scales ( $\Pi_{sst}/2 = 1$  h) respec-  
 249 tively (Stephens et al., 2019). Meanwhile, their smoothed time derivatives, indicated by the  $D\langle \dots | / Dt$   
 250 notation, eq. (2) and eq. (4), are defined using two half cosine masks as described in Sitnov et  
 251 al. (2012). The fifth parameter, eq. (5), uses an exponential function to smooth over  $vB_s^{IMF}$  (where  
 252  $B_s^{IMF} = -B_z^{IMF}$  when  $B_z^{IMF} < 0$  and  $B_s^{IMF} = 0$  otherwise). The exponential function not only  
 253 acts as a smoothing window but also captures the loading of magnetic flux in the lobes during  
 254 the substorm growth phase, thus, the e-folding time,  $\tau_0 = 0.5$  h, was set based on the typical du-  
 255 ration of the growth phase (Partamies et al., 2013). Six e-foldings were used in the convolution,  
 256  $\tau_\infty = 6\tau_0$ . Note, the integration only occurs over past data, as indicated by the limits of integra-  
 257 tion in eqs. (1)–(5), to prevent non-causal effects, that is, to prevent  $\mathbf{G}$  from reacting to changes  
 258 that have not yet occurred.

259  $\mathbf{G}(t)$  is then discretized by sampling eqs. (1)–(5) at a 5-min cadence spanning the years 1995–  
 260 2020 (corresponding to the magnetometer archive time period). Thus, each 5-min moment cor-  
 261 responds to a particular point in state-space,  $\mathbf{G}(t = t_i)$ , for a total number of points  $k_{SS} \approx 2.7 \cdot$   
 262  $10^6$ . Note,  $k_{SS}$  does not generally equal the number of magnetometer records in the archive,  $k_{DB} =$   
 263  $8.6 \cdot 10^6$  from Table 1, since each state-space point may correspond to zero, one, or many mag-  
 264 netometer records. The DM reconstructions also then operate on a 5-min cadence.

### 265 2.3 Mining Data Using k-Nearest Neighbors

266 Our approach resembles the k-Nearest Neighbor (kNN) method of DM (Vassiliadis et al.,  
 267 1995; Wettschereck et al., 1997), but also has important distinctions (Sitnov et al., 2008; Stephens  
 268 et al., 2019). First, while the kNN subsets are first identified in the state-space, the magnetic field  
 269 reconstruction is performed in the real space using magnetometer observations that occurred dur-  
 270 ing those  $k_{NN}$  moments. The choice of the number of  $k_{NN}$  must be ample enough to fit flexible  
 271 magnetic field models with high degrees of freedom (Tsyganenko & Sitnov, 2007; Stephens et  
 272 al., 2019) while at the same time sufficiently small,  $1 \ll k_{NN} \ll k_{SS}$ , as to provide adequate sen-  
 273 sitivity to the storm and substorm phases. Second, the state-space includes the smoothed time  
 274 derivatives of the activity indices to increase the sensitivity of the DM procedure to these phases  
 275 and to capture memory effects of the magnetosphere as a dynamic system (Sitnov et al., 2001).

276 Consider a particular moment of interest,  $t = t^{(q)}$ , which corresponds to a query point in  
 277 state-space  $\mathbf{G}^{(q)} = \mathbf{G}(t^{(q)})$ . The distance,  $R_q^{(i)}$ , between each other state-space point,  $\mathbf{G}^{(i)}$ , and  
 278  $\mathbf{G}^{(q)}$  is then defined using the Euclidean distance metric:

$$R_q^{(i)} = \sqrt{\sum_{k=1}^5 \left( G_k^{(i)} - G_k^{(q)} \right)^2 / \sigma_{G_k}^2}, \quad (6)$$

279 where each state-space component,  $G_k$  from eqs. (1)–(5), is standardized by dividing by its stan-  
 280 dard deviation  $\sigma_{G_k}$  (computed over the entirety of the state-space). The  $k_{NN}$  closest points in state-  
 281 space thus form the NN subset for  $t = t^{(q)}$ .

282 Since the number of state-space points,  $k_{SS}$ , is quite large, the number of our instance-based  
 283 subset  $k_{NN}$  can also be made sufficiently large to use for the magnetic field reconstruction a suf-  
 284 ficiently flexible model with many degrees of freedom, which is described in the next section.  
 285 The specific value of  $k_{NN} = 32,000$  ( $\sim 1\%$  of  $k_{SS}$ ) used in this study was found before to pro-  
 286 vide good validation results and resolve the spatial structure of the magnetic field and its evolu-  
 287 tion during substorms without overfitting (Stephens et al., 2019; Sitnov, Stephens, et al., 2019;  
 288 Stephens & Sitnov, 2021). Recall, each NN corresponds to a particular moment, thus adjacent  
 289 NNs form intervals in time when the magnetosphere was presumably in a similar state. Those  
 290 time intervals are then used to extract a subset of magnetometer records from the archive (Ta-  
 291 ble 1). The number of records in the magnetometer subset,  $S_{NN}$ , again is not generally equal to  
 292  $k_{NN}$  as it depends on the number of probes available at any NN moment. Typical values of  $S_{NN}$   
 293 for this study are  $S_{NN} \approx 9 \cdot 10^5$ .

294 The model architecture (section 2.4) is then fit by minimizing the weighted RMS differ-  
 295 ence between the observed and modeled magnetic field vectors over the kNN subset:

$$M_{err}^{(NN)} = \sqrt{\sum_{j \in S_{NN}} \sum_{i=x,y,z} w_j w_{(0)}(r) \left[ B_i^{(mod)}(\mathbf{r}^{(j)}) - B_i^{j,obs} \right]^2}, \quad (7)$$

296 where  $B_i^{j,obs}$  is the magnetic field record from the kNN subset and  $B_i^{(mod)}(\mathbf{r}^{(j)})$  is the value of the  
 297  $i$ th magnetic field component of the model evaluated at the spacecraft location of  $j$ th NN obser-  
 298 vation  $\mathbf{r}^{(j)}$ .

299 Note that the data points in the objective function eq. (7) are weighted by two factors,  $w_j$   
 300 and  $w_{(0)}(r)$ , with the latter acting to mitigate the inhomogeneity of magnetometer records in the  
 301 real space, which is seen from Figure S1. In this weighting procedure, which is described in more  
 302 detail in Tsyganenko and Sitnov (2007), the data is binned into  $0.5R_E$  intervals of the geocen-  
 303 tric distance  $r$ . Then the weight  $w_{(0)}(r)$  is calculated as  $\langle \Delta N \rangle / \max \{0.2\langle \Delta N \rangle, \Delta N_i\}$ , where  $\Delta N_i$   
 304 is the number of data points in the  $i$ th bin and  $\langle \Delta N \rangle$  is the average number per bin over the en-  
 305 tire set.

306 The other weighting,  $w_j$ , distance-weights each magnetometer record based on its corre-  
 307 sponding NN's distance,  $R_q^{(i)}$ , to the query point,  $\mathbf{G}^{(q)}$ , in the state-space using a Gaussian func-  
 308 tion:

$$w_j = \exp \left[ -\frac{1}{2} \left( \frac{R_q^{(j)}}{\sigma R_{NN}} \right)^2 \right]. \quad (8)$$

309  $R_{NN}$  is the radius of the NN sphere defined as the distance between the query point  $\mathbf{G}^{(q)}$  and the  
 310 furthest NN:  $R_{NN} = \max \{R_q^{(i)}\}$ . This weighting scheme gives higher weights to data points that  
 311 are presumably more similar to the event of interest which also mitigates kNN's bias towards weaker  
 312 events caused by the inhomogeneity of data in the state-space (Stephens et al., 2020). The spe-  
 313 cific value of the weighting parameter  $\sigma = 0.3$  used in this study was found in earlier studies to  
 314 improve the spatial reconstruction and avoid overfitting for the chosen value of  $k_{NN}$ .

315 **2.4 Model Magnetic Field Architecture**

316 The analytical description of the magnetospheric magnetic field used in this study is sim-  
 317 ilar to that of earlier empirical reconstructions of substorms and is described in more detail in (Stephens  
 318 et al., 2019) (the only differences are the variable TCS structure and the adoption of the “bowl-  
 319 shaped” deformation as discussed below). The total magnetospheric magnetic field,  $\mathbf{B}_{tot}$ , can be  
 320 described as a summation of fields owing to individual current systems:  $\mathbf{B}_{tot} = \mathbf{B}_{int} + \mathbf{B}_{FAC} +$   
 321  $\mathbf{B}_{eq} + \mathbf{B}_{MP}$ . The internal field,  $\mathbf{B}_{int}$ , generated by currents deep in the Earth’s interior, is repre-  
 322 sented by the IGRF model (Alken et al., 2021). Of interest are the magnetic fields generated by  
 323 currents flowing within geospace, termed the external field,  $\mathbf{B}_{ext}$ . Specifically here, assuming the  
 324 magnetopause as a perfectly conducting layer, the set of current systems is limited to those flowing  
 325 within the magnetopause, the field-aligned currents  $\mathbf{B}_{FAC}$  and equatorial currents  $\mathbf{B}_{eq}$ , and on  
 326 the magnetopause  $\mathbf{B}_{MP}$ .

327 The building block for the equatorial current systems is the general magnetic vector po-  
 328 tential solution of a thin current sheet,  $\mathbf{A}_{sheet}$ , as detailed by Tsyganenko and Sitnov (2007). Solved  
 329 in cylindrical coordinates  $(\rho, \phi, z)$ , the solution is composed of a Fourier series in  $\phi$  and a Fourier-  
 330 Bessel series in  $\rho$ , and the resulting magnetic field,  $\mathbf{B}_{sheet} = \nabla \times \mathbf{A}_{sheet}$ , is given by a basis func-  
 331 tion expansion having the form:

$$\mathbf{B}_{sheet}(\rho, \phi, z) = \sum_{n=1}^N a_{0n}^{(s)} \mathbf{B}_{0n}^{(s)} + \sum_{m=1}^M \sum_{n=1}^N (a_{mn}^{(o)} \mathbf{B}_{mn}^{(o)} + a_{mn}^{(e)} \mathbf{B}_{mn}^{(e)}), \quad (9)$$

332 where  $\mathbf{B}_{0n}$ ,  $\mathbf{B}_{mn}^{(o)}$ , and  $\mathbf{B}_{mn}^{(e)}$  are basis functions with axially symmetry, odd (sine), and even (co-  
 333 sine) symmetry respectively; while  $a_{mn}$  are the amplitude coefficients. Defining the magnetic field  
 334 as the curl of a magnetic vector potential ensures a divergenceless magnetic field and allows for  
 335 modifications to the current sheet structure discussed below.

336 Note, although this yields an arbitrary description in  $\rho$  and  $\phi$ , its structure in  $z$  is rigidly  
 337 defined to be an infinitely thin current sheet at  $z = 0$ . However, the Dirac delta profile of the cur-  
 338 rent density in  $z$  can be broadened into a realistic finite distribution by performing the variable  
 339 substitution  $\zeta = \sqrt{z^2 + D^2}$ , introducing the parameter  $D$  as the current sheet half-thickness. Note,  
 340 the thickness parameter  $D$  need not be a constant but can take the form of a differentiable func-  
 341 tion  $D = D(\rho, \phi)$ .

342 A distinctive feature of the magnetotail is the formation of multiscale current sheets in the  
 343 substorm growth phase with an ion-scale thin current sheet (TCS) embedded into a much thicker  
 344 current sheet (Sergeev et al., 2011). In order to capture this feature, Stephens et al. (2019) used  
 345 two such expansions to describe the equatorial field:

$$\mathbf{B}^{(eq)}(\rho, \phi, z) = \mathbf{B}^{(eq)}(\rho, \phi, z; D) + \mathbf{B}^{(eq)}(\rho, \phi, z; D_{TCS}), \quad (10)$$

346 where  $D_{TCS}$  is constrained to be  $D_{TCS} < D$ . Further studies (Stephens et al., 2019; Sitnov, Stephens,  
 347 et al., 2019) confirmed the buildup of TCS in the growth phase of substorms and their decay dur-  
 348 ing the expansion and recovery phases.

349 These earlier studies assumed a spatially constant TCS thickness,  $D_{TCS} = \text{const}$ , although  
 350 it was allowed to vary in time (Stephens et al., 2019). Here, the embedded TCS structure has been  
 351 further generalized to verify the possible physical mechanisms of the TCS formation. It can be  
 352 explained, (e.g., Sitnov et al., 2006), by figure-eight like Speiser (1965) proton orbits. If this is  
 353 the case, the parameter  $D_{TCS}$  of the magnetic field model should depend on the distance  $\rho$  from  
 354 the Earth because the Speiser orbit size,  $\rho_{Si}$ , is inversely proportional to the magnetic field out-  
 355 side the sheet,  $B_L$ , which itself depends on  $\rho$  (Wang et al., 2004). To take this effect into account,  
 356 the TCS half-thickness from eq. (10) is represented by:

$$D_{TCS}(x, y) = \left( \alpha e^{-\beta \rho'} + D_0^{-1} \right)^{-1}, \rho' = \sqrt{(x - x_0)^2 + y^2}. \quad (11)$$

357 This functional form of the TCS introduces four free parameters,  $\alpha$ ,  $\beta$ ,  $D_0$ , and  $x_0$ .  $D_{TCS}$   
 358 asymptotically approaches a value of  $D_0$  as  $\rho$  gets large and is constrained to be  $D_0 < D$ . The  
 359  $\alpha$  parameter, which must be positively valued, shifts the curve along  $\rho$ , with small values, e.g.,  
 360  $\alpha \approx 0.001$ , resembling a constant curve  $D_{TCS} = D_0$ , while larger values move the curve to larger  
 361 values of  $\rho$ . Meanwhile the  $\beta$  parameter affects how gradually the curve approaches  $D_0$ , with  
 362 smaller/larger values corresponding to a more gradual/abrupt transition. The fourth parameter,  
 363  $x_0$ , allows  $D_{TCS}$  to shift along the Sun-Earth line.

364 A further complication is that the equatorial current system rarely lies in a plane centered  
 365 about  $z = 0$ . The Earth's dipole axis is not generally orthogonal to the direction of the solar wind  
 366 flow. The angle that the dipole axis makes with the Z axis of the GSM coordinate system is the  
 367 “dipole tilt angle”. Its non-zero value may cause bending and warping of the tail current sheet  
 368 while changes in the IMF clock angle (the angle between geomagnetic north and the projection  
 369 of the IMF vector onto the GSM Y-Z plane) may twist the current sheet (Tsyganenko & Fairfield,  
 370 2004; Tsyganenko et al., 2015). These effects can be accounted for by application of the general  
 371 deformation technique (Tsyganenko, 1998). Specifically, here the “bowl-shaped” deformation  
 372 from Tsyganenko (2014) is used, introducing three additional free parameters which define the  
 373 center of the current sheet; the hinging distance  $R_H$ , the warping parameter  $G$ , and the twisting  
 374 parameter  $TW$ .

375 The values of  $M$  and  $N$  determine the number of azimuthal and radial expansions in eq. (9)  
 376 respectively and thus the resolution of the equatorial currents in  $\phi$  and  $\rho$  respectively. Here, as  
 377 with previous substorm investigations (Stephens et al., 2019),  $(M, N) = (6, 8)$  as this was deter-  
 378 mined a sufficient resolution to resolve current structure throughout the near and mid-tail with-  
 379 out overfitting to data (Stephens & Sitnov, 2021). Further, as with the prior investigations, in or-  
 380 der to account for potential dynamical pressure effects on the structure of equatorial currents, each  
 381 of the amplitude coefficient terms in eq. (9) are made explicit functions of  $P_{dyn}$ :  $a_{\alpha\beta}^{(\gamma)} = a_{0,\alpha\beta}^{(\gamma)} +$   
 382  $a_{1,\alpha\beta}^{(\gamma)} \sqrt{P_{dyn}}$ , doubling their number. The end result is a total of 416 amplitude coefficients which  
 383 determine the spatial structure of the equatorial current sheet.

384 The FAC magnetic field,  $\mathbf{B}_{FAC}$ , module used in this study is identical to that of Stephens  
 385 et al. (2019). The foundation of their analytical description are the radially flowing conical cur-  
 386 rent systems developed in Tsyganenko (1991), which are then bent to follow approximately dipole-  
 387 lar field lines using the general deformation technique which also accounts for the day-night asym-  
 388 metry (Tsyganenko, 2002a). The azimuthal dependence of the conical currents utilizes a Fourier  
 389 series, giving them flexibility to reconstruct the magnetic local time variations of the FACs but  
 390 at the expense of having a very rigid latitudinal structure. In order to mimic expansion like flex-  
 391 ibility in latitude, four such conical current systems are placed at overlapping latitudes. The first  
 392 four Fourier terms are used for each of the four latitudinal varying conical currents resulting in  
 393 a total of 16 linear amplitude coefficients that determine the FACs spatial structure. Global rescal-  
 394 ing parameters were introduced to allow the FACs to shrink and grow in response to storm and  
 395 substorm phases. Instead of allowing each of the four current systems to rescale independently,  
 396 the two higher latitude systems were tied to one parameter  $\kappa_{R1}$  and the two lower to another  $\kappa_{R2}$ .  
 397 The values of  $\kappa_{R1}$  and  $\kappa_{R2}$  were constrained so that they approximated the region-1 and region-  
 398 2 current systems respectively. This formulation was shown to successfully reproduce the more  
 399 complex spiral like FAC pattern observed in the AMPERE data (Sitnov et al., 2017).

400 Unlike the other external fields, in which the magnetic field sought is consistent with some  
 401 conceptualization of a current system, the magnetopause magnetic field,  $\mathbf{B}_{MP}$ , does not attempt  
 402 to represent a current. Instead, the domain of validity of the model is restricted to just inside the  
 403 magnetopause current layer, where  $\mathbf{j}_{MP} = 0$ . Thus,  $\mathbf{B}_{MP}$  is irrotational and can be represented  
 404 by a magnetic scalar potential,  $\mathbf{B}_{MP} = -\nabla U$  and its formulation is simply the solution to Laplace's  
 405 equation:  $\nabla^2 U = 0$  (Tsyganenko, 2013). In this context,  $\mathbf{B}_{MP}$  is termed a shielding field in that  
 406 it ensures the magnetosphere is closed, that is, that field lines do not cross the magnetopause. A  
 407 closed magnetosphere is represented by the condition  $\mathbf{B}_{tot} \cdot \mathbf{n}|_S = 0$ , where  $S$  is the modeled mag-  
 408 netopause boundary and  $\mathbf{n}$  is the normal to that surface. Here, as with previous studies,  $S$  is de-

409 fined as the Shue magnetopause (Shue et al., 1998). In practice it is more tractable to represent  
 410  $\mathbf{B}_{MP}$  as a combination of shielding fields:  $\mathbf{B}_{MP} = \mathbf{B}_{int}^{(sh)} + \mathbf{B}_{FAC}^{(sh)} + \mathbf{B}_{eq}^{(sh)}$ ; that way, each shield-  
 411 ing field can be formulated independently using a coordinate system and geometry that makes  
 412 sense for that particular system. For example, owing to the cylindrical geometry of  $\mathbf{B}_{eq}$ ,  $U_{eq}$  is  
 413 represented by an expansion of Fourier-Bessel harmonics (eq. 20 of Tsyganenko & Sitnov, 2007),  
 414 while  $U_{int}$  and  $U_{FAC}$  utilize an expansion of “Box” harmonics, appendix of Tsyganenko (1998)  
 415 and eq. 34 of Tsyganenko (1995) respectively. The coefficients of the shielding field expansion  
 416 are found by minimizing the normal component of the combined field at the magnetopause bound-  
 417 ary, e.g.,  $\min \left[ (\mathbf{B}_{eq,j} + \mathbf{B}_{eq,j}^{(sh)}) \cdot \mathbf{n}_j \right]$ . For a more thorough discussion on this topic see Tsyganenko  
 418 (2013).

419 One more consideration built into the structure of the model is the magnetosphere’s ex-  
 420 pansion and contraction in response to changes in the solar wind dynamical pressure,  $P_{dyn}$ . It is well  
 421 established from observations of magnetopause crossings that the magnetopause responds to de-  
 422 creases/increases in  $P_{dyn}$  by expanding/contracting in a self-similar way, that is, its size changes  
 423 but not its shape (e.g., Sibeck et al., 1991; Shue et al., 1998). This self-similarity is easily rep-  
 424 resented by rescaling the position vector as a function of  $P_{dyn}$ . Using simple pressure balance con-  
 425 siderations the functional form of this rescaling is  $\mathbf{r}' = P_{dyn}^{-\kappa} \mathbf{r}$ , where  $\kappa = 1/6$  for a perfect dipole  
 426 (Mead & Beard, 1964). Here, as with many previous empirical studies, all current systems are  
 427 assumed to possess the same self-similarity rescaling, that is they all take the same functional form  
 428 and same value of  $\kappa$  (Tsyganenko, 2013). This assumption simplifies the shielding of these fields  
 429 as both the shielded and the shielding fields rescale together.  $\kappa$  could be treated as a free param-  
 430 eter when the model is fit to data, however, previous studies have shown  $\kappa$  to be relatively sta-  
 431 ble (Tsyganenko, 2002b), so here a constant value of  $\kappa = 0.155$  from Tsyganenko and Sitnov  
 432 (2007) was used.

433 To summarize, the final magnetic field model configuration includes 432 linear amplitude  
 434 coefficients and 10 free non-linear parameters  $D$ ,  $\alpha$ ,  $\beta$ ,  $D_0$ ,  $x_0$ ,  $R_H$ ,  $G$ ,  $TW$ ,  $\kappa_{R1}$ , and  $\kappa_{R2}$  which  
 435 are determined by fitting them to the identified subset of magnetometer data. The linear coeffi-  
 436 cients are determined by applying the singular value decomposition pseudo-inversion method  
 437 to the overdetermined linear least squares problem (Jackson, 1972; Press et al., 1992). The non-  
 438 linear parameters are found by embedding the linear solver within the Nelder-Mead downhill sim-  
 439 plex algorithm (Nelder & Mead, 1965).

### 440 3 Ion Diffusion Regions and Reconstructed Global Reconnection Structures

#### 441 3.1 Reconnection Features in the Equatorial Plane

442 The main goal of the MMS mission (Burch, Moore, et al., 2016) was the detection and in-  
 443 vestigation of reconnection regions in the magnetosphere and its boundary. That goal was rel-  
 444 atively easy to achieve at the magnetopause because of its regular structure (Fuselier et al., 2011)  
 445 and in the magnetosheath due to multiple reconnection sites in its turbulent plasma volume (Phan  
 446 et al., 2018). By contrast, only a handful of fortunate X-line encounters were detected/investigated  
 447 in the magnetotail (Torbert et al., 2018; Chen et al., 2019). In this regard, the proposed DM re-  
 448 constructions offer an attractive opportunity to explore the dynamics of magnetotail topology on  
 449 a global scale, and its fidelity can be demonstrated by comparing our results with MMS obser-  
 450 vations. Magnetic reconnection can be directly observed if and when a spacecraft fortuitously  
 451 flies through an Ion Diffusion Region (IDR), as shown in Figure 1. A recent systematic survey  
 452 of MMS plasma and field data in 2017 (Rogers et al., 2019) identified 12 such magnetotail IDRs,  
 453 defined as correlated reversals of the proton bulk flow velocity,  $v_x$ , and the North-South magnetic  
 454 field,  $B_z$ , as shown in the Figure 1 inset, along with additional Hall magnetic and electric field  
 455 signatures. That analysis was later extended to 2018–2020 for a total of 26 IDR events (Rogers  
 456 et al., 2021) labeled here A–Z, “IDR alphabet”, listed in Table 2. The second column in the ta-  
 457 ble lists the starting date and time of each IDR interval found in Rogers et al. (2021). Due to the  
 458 5-min cadence of our DM approach, the actual reconstructed times are rounded to the nearest 5-  
 459 min as indicated in the third column.

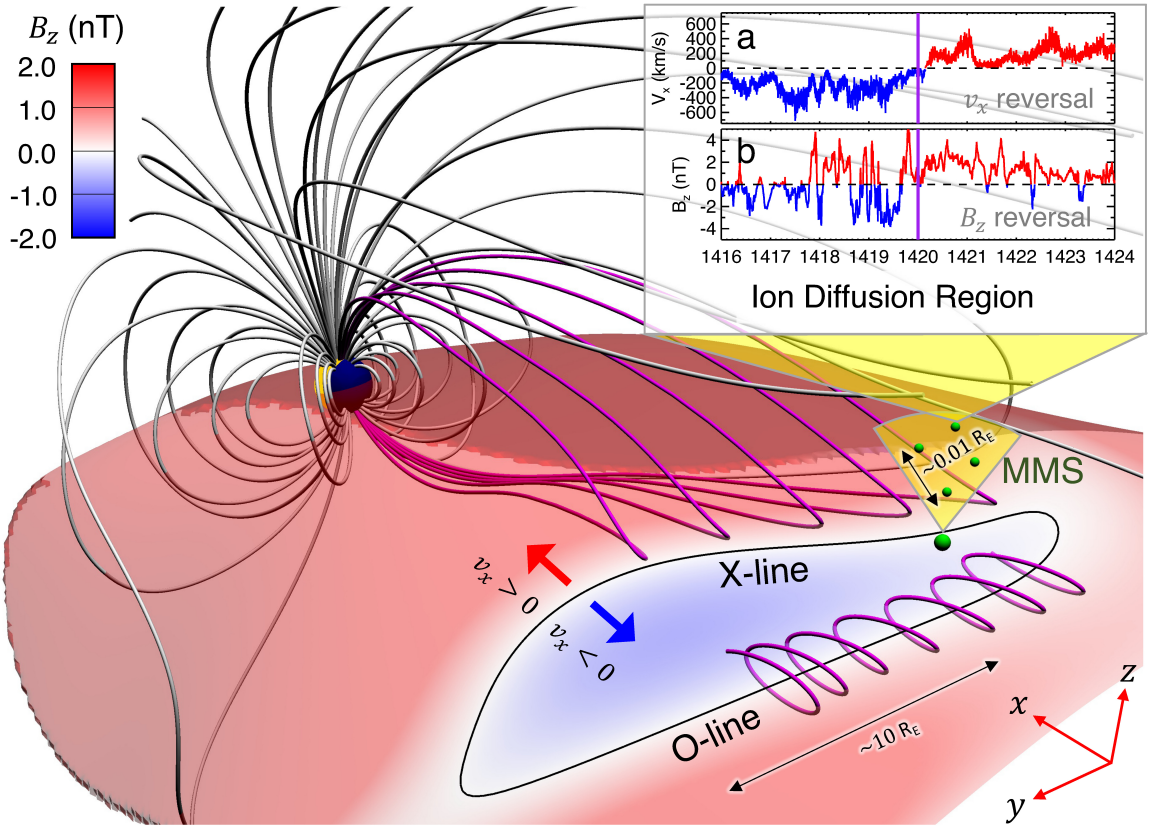


**Figure 1.** 3D global picture of the magnetosphere and local MMS observations for 5 August 2020 (event Y in Table 2) in GSM coordinates. It shows that the data mining reconstructed X-line matches one of 26 ion diffusion region (IDR) encounters observed by the MMS mission during 2017–2020. It includes selected field lines and the color-coded magnetic field distribution,  $B_z$ , sampled at the center of the tail current sheet taking into account deformation effects caused by the tilt angle of the Earth's dipole axis. The  $B_z = 0$  isocontour is shown by the black line (the color table is saturated at  $|B_z| = 2$  nT to better reveal the isocontour). The inset shows key IDR parameters: (a) the proton bulk flow velocity component  $v_x$  and (b) the magnetic field  $B_z$ , from the MMS4 probe (the small green spheres show the MMS tetrahedral configuration) whose location is marked by the larger green sphere near the equatorial plane. The purple vertical line marks the reconstruction moment, 5 August 2020, 14:20 UT. The 3D visualizations are constructed using the VisIt visualization tool (Childs et al., 2012).

460 The DM reconstruction of the magnetic field for event Y in the early expansion phase of  
 461 the 5 August 2020 substorm (Figure 1) shows the formation of an X-line at  $r \approx 23R_E$  in the tail  
 462 within  $\sim 1R_E$  from the corresponding IDR marked by the large green circle. This data-derived  
 463 image of the X-line resembles sketches of solar flare arcades (e.g., Shiota et al., 2005) but with  
 464 a fundamental advantage that it is backed by a quantitative description. The X-line appears on  
 465 the dusk flank of the tail illustrated as the earthward part of the  $B_z = 0$  isocontour in the equa-  
 466 torial plane (black line). It also corresponds to an earthward edge of a relatively long ( $25R_E$ ) spi-  
 467 ral structure, shown by the sample field lines that encircle the tailward part of the  $B_z = 0$  isocon-  
 468 tour and form a magnetic O-line.

469 The projection of the magnetic field at the center of the tail current sheet into the equato-  
 470 rial plane is displayed in Figure 2D showing that the  $B_z = 0$  contour passes within  $\sim 1R_E$  of the  
 471 IDR observed by MMS. This success is remarkable given that only  $\sim 0.03\%$  (32 of the 105,975)  
 472 of the measurements used to reconstruct the magnetic field were taken from this event, with the  
 473 other 99.97% coming from other similar events identified using the above described DM approach.  
 474 The reconstructions of three other events (G, M, W) presented in Figure 2 also show the  $B_z =$   
 475 0 contours pass within  $\sim 1R_E$  of the observed IDRs. Closer examination shows that only events G,  
 476 W, and Y are X-lines, whereas event M corresponds to an O-line. Indeed, since the microscale  
 477 formation of the MMS tetrahedron cannot determine X-line motions using timing analysis, (e.g.,  
 478 Eastwood et al., 2010), or by framing the X-lines by being tailward and earthward of them (Angelopoulos  
 479 et al., 2008), it cannot distinguish whether they are X- or O-lines.

**Table 2.** The MMS IDR Alphabet.

Event	Start Date/Time	Model Date/Time	$D_{0nT}(R_E)$	$D_{2nT}(R_E)$	Figures
A	2017-05-28T03:57	03:55	1.94	1.40	S2 S8
B	2017-07-03T05:26	05:25	4.72	3.23	S7 S13
C	2017-07-06T15:34	15:35	0.58	3.77	S2 S8
D	2017-07-06T15:45	15:45	1.72	2.54	S2 S8
E	2017-07-11T22:33	22:35	1.37	1.46	S2 S8
F	2017-07-17T07:48	07:50	8.62	5.78	S7 S13
G	2017-07-26T00:02	00:00	1.44	1.24	F2 F3
H	2017-07-26T07:00	07:00	1.91	1.63	S3 S9
I	2017-07-26T07:27	07:25	5.18	0.39	S5 S11
J	2017-08-06T05:13	05:15	7.70	0.63	S5 S11
K	2017-08-07T15:37	15:35	3.22	1.57	S5 S11
L	2017-08-23T17:53	17:55	1.88	0.54	S3 S9
M	2018-08-15T11:57	11:55	1.47	0.70	F2 F3
N	2018-08-26T06:38	06:40	2.85	2.17	S5 S11
O	2018-08-27T11:39	11:40	0.95	1.65	S3 S9
P	2018-08-27T12:14	12:15	7.43	1.19	S6 S12
Q	2018-09-10T17:14	17:15	0.78	1.02	S3 S9
R	2018-09-10T23:57	23:55	0.88	1.64	S4 S10
S	2019-07-25T21:40	21:40	1.45	4.26	S4 S10
T	2019-08-31T12:01	12:00	1.88	0.68	S6 S12
U	2019-09-06T04:38	04:40	3.57	0.77	S6 S12
V	2020-08-02T16:58	17:00	1.06	0.61	S4 S10
W	2020-08-02T17:09	17:10	0.65	0.55	F2 F3
X	2020-08-03T01:04	01:05	1.03	2.11	S4 S10
Y	2020-08-05T14:19	14:20	1.13	3.94	F2 F3
Z	2020-08-29T09:56	09:55	3.26	1.73	S6 S12

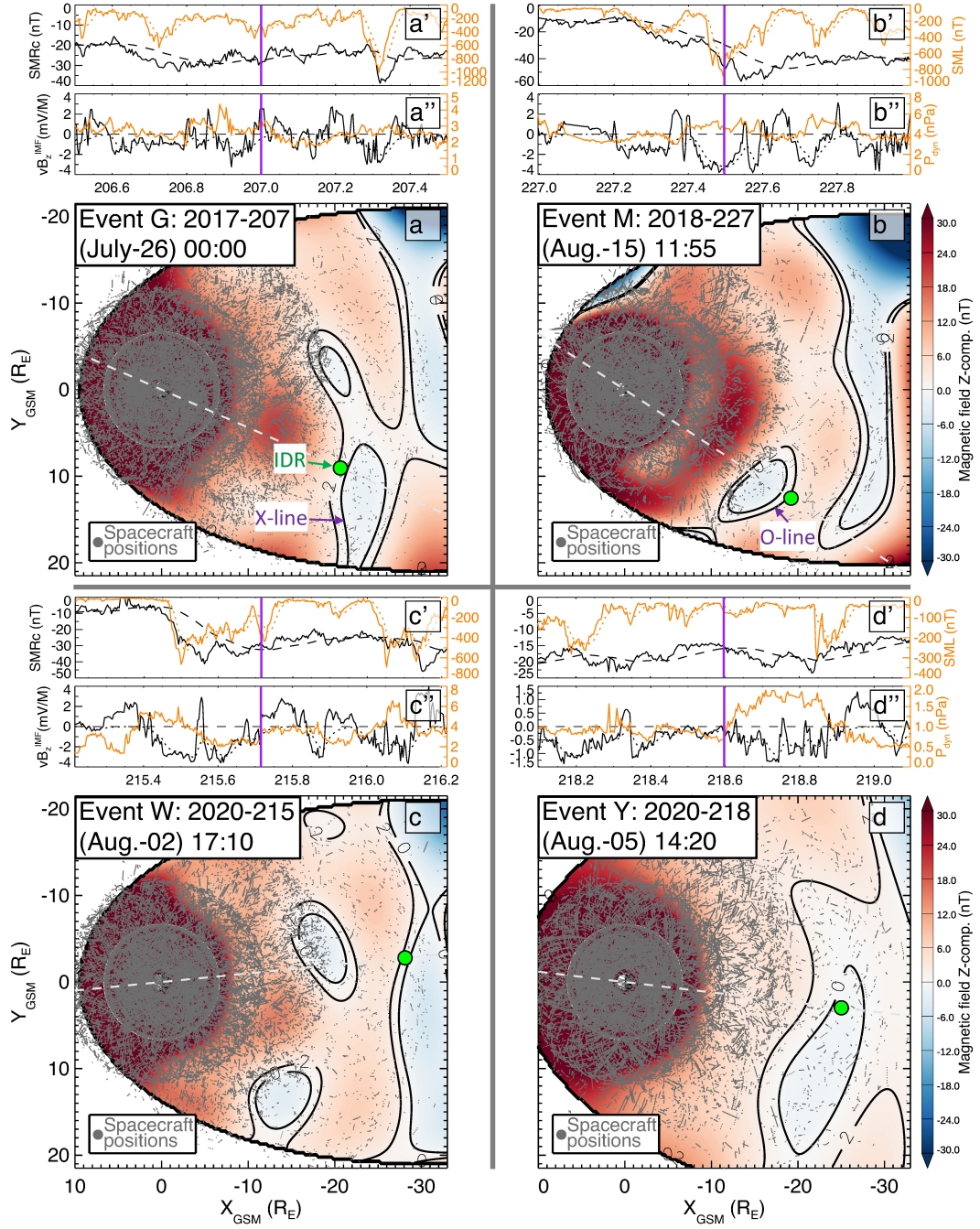


**Figure 2.** IDRs and the equatorial magnetic field landscape. (a–d) Color-coded distributions of the equatorial magnetic field,  $B_z$ , with  $B_z = 0$  and  $2 \text{ nT}$  isocontours (black lines), large green dots pointing to the IDRs, and gray dots showing the spacecraft positions for the NN subsets used in the DM method for four IDR events, G, M, W and Y. Panels on top of each equatorial  $B_z$  distribution show the global context of the considered events in terms of (a'–d') the storm and substorm indices SMRC (black), SML (orange), and (a''–d'') the solar wind/IMF parameters  $vB_z^{\text{IMF}}$  (black) and  $P_{\text{dyn}}$  (orange) with the purple vertical line marking the event time.

480 The fourth column of Table 2 specifies the computed distance,  $D_{0nT}$ , between each MMS  
 481 observed IDR event and the reconstructed  $B_z = 0$  nT contour (distance is found as the minimum  
 482 radius of the 3D sphere originating from the MMS tetrahedron which crosses the correspond-  
 483 ing  $B_z = \text{const}$  contour). This demonstrates that the consistency of the DM reconstructions are  
 484 not isolated to just the events displayed in Figure 2. Indeed we can categorize 16 of our DM re-  
 485 constructions as “Hits”, that is  $D_{0nT} < 2.0R_E$ , which includes 11 X-lines (A, C, D, E, G, Q, S,  
 486 V, W, X, Y) and 5 O-lines (H, L, M, O, R). The equatorial X-line reconstructions for four of these  
 487 events have been shown in Figure 2 while the analogous figures for the other 12 events are con-  
 488 tained in the Supporting Information (Figures S2–S4).

489 Several more event reconstructions do not fully resolve the  $B_z = 0$  nT contour in the vicinity  
 490 of the observed IDR, but still resolve regions of small  $B_z$  near the IDR. To categorize these  
 491 events, the distance,  $D_{2nT}$ , between the observed IDR and the  $B_z = 2$  nT contour is displayed  
 492 as the fifth column in Table 2. This yields 8 “Near Hits” (I, J, K, N, P, T, U, Z) where  $D_{2nT} <$   
 493  $2.2R_E$  ( $< 2R_E$  for all events except N). The equatorial  $B_z$  for these events are shown in Figures S5  
 494 and S6.

495 The two “Misses” (B, F) are then events where both  $D_{0nT} \geq 2.0R_E$  and  $D_{2nT} \geq 2.2R_E$   
 496 and are shown in Figure S7. However, both events have a plausible explanation. Event B occurs  
 497 during weak magnetospheric activity ( $SML \approx 0$ ) with effectively no solar wind/IMF input ( $vB_z^{IMF} >$   
 498 0) while event F takes place during the middle of a several hours long gap in solar wind and IMF  
 499 data (they are interpolated in the reconstruction). The last column in Table 2 matches each IDR  
 500 event to its corresponding figures.

### 501 3.2 Reconnection Features in the Meridional Planes

502 The corresponding meridional slices through the planes containing the IDRs of the Fig-  
 503 ure 2 events (G, M, W, Y) are shown in Figure 3, illustrating the magnetic topology and distri-  
 504 butions of electric currents, while the remainder of the IDR alphabet (Figures S2–S7) is shown  
 505 in Figures S8–S13. The figures clarify that the observed  $B_z = 0$  contours indeed represent X-  
 506 and O-lines similar to the 3D magnetotail field geometry shown in Figure 1. They also confirm  
 507 the quasi-2D nature of reconnection apparently imposed by the North-South symmetry of the mag-  
 508 netotail (e.g., Tsyganenko & Fairfield, 2004) which is drastically different from the inherently  
 509 3D reconnection processes in the solar corona (Liu et al., 2016) and rapidly rotating planets (Griton  
 510 et al., 2018).

511 These meridional distributions resemble empirical visualizations of reconnection in lab-  
 512 oratory plasmas, which became possible due to their large number of real probes (up to 200) and  
 513 additional symmetry constraints, such as the cylindrical symmetry imposed by the toroidal-shaped  
 514 flux cores in the PPPL Magnetic Reconnection Experiment (MRX) (Ji et al., 2022). Still, in con-  
 515 trast to MRX, magnetotail reconnection is only quasi 2D due to the finite length of the X-line form-  
 516 ing a closed loop with the O-line, as well as the explicit 3D effects, such as null-points (e.g., Greene,  
 517 1988; Ji et al., 2022). Null-points in the tail were indeed inferred from the four-probe Cluster ob-  
 518 servations (Xiao et al., 2006). They have also been extensively discussed as a key element of the  
 519 substorm onset mechanism in global MHD simulations (Tanaka et al., 2021). An example of the  
 520 null-point pair seen in our DM reconstruction of event Y is presented in Figure S14. Additional  
 521 deviations from the simple 2D picture could be due to a strong IMF  $B_y$  (e.g., Cowley, 1981) or  
 522 North-South oscillations of the tail current sheet that resemble a flapping flag (e.g., Sergeev et  
 523 al., 2006; Sitnov, Birn, et al., 2019).

524 Another interesting feature of the meridional reconstructions, which has important physics  
 525 implications, is evident in Figure 3. It shows the variable thickness of the TCS assumed by eq. (11)  
 526 resulting in a gradually thickening TCS at further distances down the tail. This is further illus-  
 527 trated in Figure 4, where the reciprocal of the TCS half-thickness,  $1/D_{TCS}$ , (orange lines in the  
 528 main part of each panel) is compared here with the the tail lobe field  $B_L$  evaluated at  $z = 5R_E$   
 529 (black lines) for the main group of IDR events (G, M, W, Y). The similarity of orange and black  
 530 lines throughout the tail region  $-30R_E \leq x \leq -10R_E$  suggests the scaling  $D_{TCS} \propto B_L^{-1}$  is for-

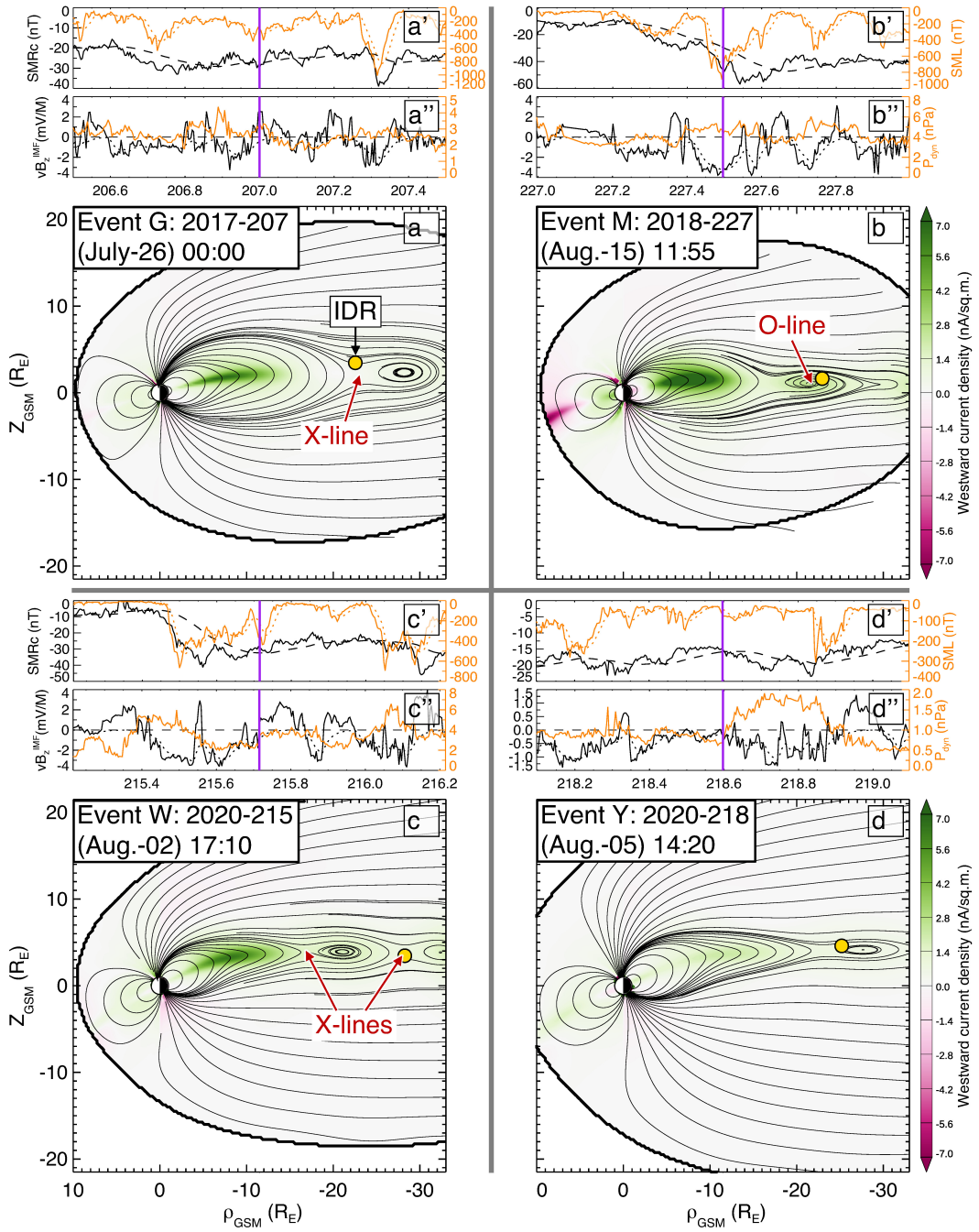


**Figure 3.** IDRs against the meridional current and magnetic field distributions. (a–d) Color-coded distribution of the electric current perpendicular (westward positive) to the meridional plane, which contains the corresponding IDR (white dashed lines in Figure 2), for four events shown in Figure 2 with the similar format for global parameters (a'–d') and (a''–d'') on top of each distribution. The IDRs are shown here by large orange dots. Thin and thick lines show the magnetic field lines and the magnetospheric boundary (magnetopause).

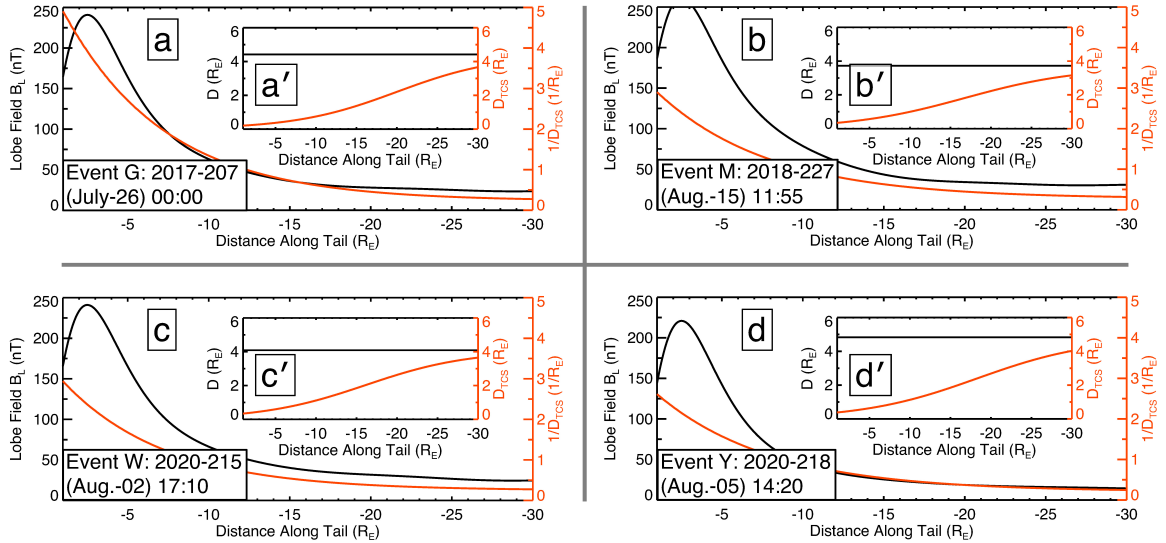


**Figure 4.** Profiles of the lobe field  $B_L$  and current sheet thicknesses along the tail. (a–d) 1D profiles of the for  $B_L$  (black line) and the inverse TCS thickness  $1/D_{TCS}$  (orange line) sampled at midnight ( $y = 0$ ) along the tail for four IDR events, G, M, W, and Y.  $B_L$  is evaluated at a height of  $z = 5R_E$  above the center of the current sheet. The inset panels (a'–d') show the value 1D profiles of the current sheet thickness for the thick sheet (black constant line) and  $D_{TCS}$  (orange line).

mally consistent with the properties of 2D current sheet equilibria for isotropic plasmas (e.g., Sitnov & Schindler, 2010). However, closer examination reveals that the lobe field in the isotropic plasma theory should collapse with the distance from Earth given the near-Earth TCS thickness ( $D_{TCS}(\rho = 0) = 0.17 - 0.34R_E$  consistent with observations that the TCS half-thickness is comparable to the thermal ion gyroradius in the field  $B_L$  (Runov et al., 2005)) much faster compared to its profiles shown in Figure 4 and consistent with earlier statistical results (Wang et al., 2004). For instance, for 2D equilibria with the constant ratio  $B_z/B_L$  (e.g., Sitnov & Schindler, 2010; Sitnov & Merkin, 2016), the lobe field should scale as  $\exp(-(x/D_{TCS}(\rho = 0))(B_z/B_L))$ , and even with  $B_z \sim 3\text{nT}$  and  $B_L \sim 100\text{nT}$  it would collapse much faster, compared to reconstructions shown in Figure 3. Besides, the conventional 2D isotropic plasma equilibria do not explain the multi-scale structure of the tail with a TCS embedded into a thicker plasma sheet.

Meanwhile, the observed scaling  $D_{TCS} \propto B_L^{-1}$  with the actual (reconstructed from data) lobe magnetic field is quite consistent with the equilibrium theory of TCS provided by the Speiser orbits (Sitnov & Merkin, 2016). In particular, the x-scale of TCS  $L_x \sim D_{TCS}(B_L/B_z)(D/D_{TCS}) \gg D_{TCS}(B_L/B_z)$ . Thus, the present DM reconstruction supports modern kinetic TCS models taking the quasi-adiabatic dynamics of Speiser ions into account. The insets in Figure 4 show the half-thicknesses of the two current sheets represented by eq. (10) along the tail, with the constant value of the thicker sheet ( $D$  black line) plotted against the variable thickness of the TCS ( $D_{TCS}$  orange line), demonstrating that  $D_{TCS}$  approaches  $D$  at increasing tail distances but is constrained to be  $D_{TCS} < D$ . Note that we neglected the possible radial dependence of the thick current sheet thickness  $D$ , similar to eq. 11, largely to avoid overfitting. We plan to further investigate the tail current sheet structure in future studies.

### 3.3 Special Cases

Special considerations were taken in regards to events R and T. For event R, the initial reconstruction placed the location of the central plasma sheet  $\sim 3R_E$  below the MMS spacecraft during the IDR observation. Upon further inspection, the event was found to have an anomalously

large value of  $B_y^{IMF}$  over the preceding 30-min, with a value of  $\sim 8$  nT. Large magnitudes of  $y$  component of the IMF are known to significantly impact the shape of the magnetotail specifically through the twisting of the plasma sheet (Tsyganenko & Fairfield, 2004; Tsyganenko et al., 2015). Although this feature is included in the structure of the model through the warping and twisting deformation equations, via the parameter  $TW$  (Tsyganenko, 1998), its impact is presumably not captured in the storm/substorm state-space represented by eqs. (1)–(5). Indeed, computing  $TW$  using the empirical relationship from Tsyganenko and Fairfield (2004) (see their eqs. (1) and (5)), results in  $TW = 1.11 \times 10^{-2}$ , the largest magnitude across all 26 events and being a factor of two larger than the next highest and a factor of five higher than the average event. Thus, event R was reconstructed using this empirical value and not the value obtained during the fit ( $TW = 2.64 \times 10^{-3}$ ). As earlier studies were primarily concerned with the inner magnetosphere and/or the near-tail region, they probably neglected to observe this inconsistency. In future studies, particularly of the mid-tail, this issue should be remedied. One potential solution is to explicitly add a dimension to the state-space that correlates to the twisting effect, for instance the value of  $B_y^{IMF}$  itself or the IMF clock angle. However, owing to the “curse of dimensionality” (Verleyen & François, 2005), expanding the state-space may dilute its sensitivity to the storm and substorm features sought. Another solution that is potentially more robust is to exclude  $TW$  from the set of free parameters that is determined when fitting to data and instead replace it with an ad-hoc functional form such as the empirical relationship from Tsyganenko and Fairfield (2004) or Tsyganenko et al. (2015).

In event T, the original reconstruction with  $\sigma = 0.3$  underresolved the X-line, apparently because of the unusual IMF structure ( $|B_z| \sim |B_x| \sim |B_y| \sim 6$  nT). To mitigate this issue, we slightly reduced the weighting parameter to  $\sigma = 0.25$ .

#### 4 Validation and Uncertainty Quantification

Examples of in-situ validation of these global reconstructions are shown in Figure 5a–5d for the MMS4 magnetic field observations of the tail during events G, M, W, and Y (only observations from MMS4 are shown as the observations from the other three spacecraft are very similar). It reveals relatively large deviations in the magnetic field components  $B_{x,y}$  parallel to the current plane (Figs. 5a, 5b). They are likely caused by the flapping North-South motions of the current sheet as a whole (Sergeev et al., 2006) that were found in MMS observations as well (Farrugia et al., 2021). These motions are spontaneous and may appear in different phases of activity, so it is not surprising that they are not captured by the DM reconstructions. At the same time, the  $B_z$  magnetic field is reproduced even better than it appears in observations after 5-min averages (compare the black line in Figure 4C with the inset in Figure 1). Thus, hitting 24 out of 26 IDRs, achieved in this study, shows (i) how to overcome the curse of data paucity for in-situ data and (ii) presents solid evidence that not only validates our DM reconstructions, but also helps understand the reconnection mechanisms and its consequences.

The fidelity of the present reconstructions can also be seen from the uncertainty analysis presented in Figure 5e–5i. It compares five original binning parameters (black lines; eqs. (1)–(5)) of the magnetosphere with their means (dark blue lines) and standard deviations (light blue envelopes) over the NN subsets. The closeness of means to the original parameters  $G_{1–5}$  and small relative values of deviations suggest that the selected NNs closely follow the magnetospheric dynamics, especially on substorm scales (Figure 5g–5h).

#### 5 Global X-line structure in the context of substorm activity

Since the main key to the present global X-line reconstructions has been the recurring nature of substorms and storms, it is interesting to check the evolution of X-lines within a substorm cycle. Indeed, some of the considered IDRs belong to classic substorms: C and D (14:35–17:25 UT), H (06:00–08:30 UT), M (09:35–14:55 UT), U (03:00–06:00). Here we consider in more detail the July 26, 2017 substorm containing event H. The equatorial  $B_z$  distributions in the growth, expansion, and recovery phases of this substorm are shown in Figure 6 and animated with 5-min cadence in Movie S1, with event H shown in Figure 6e. The onset of this substorm (Figure 6d)

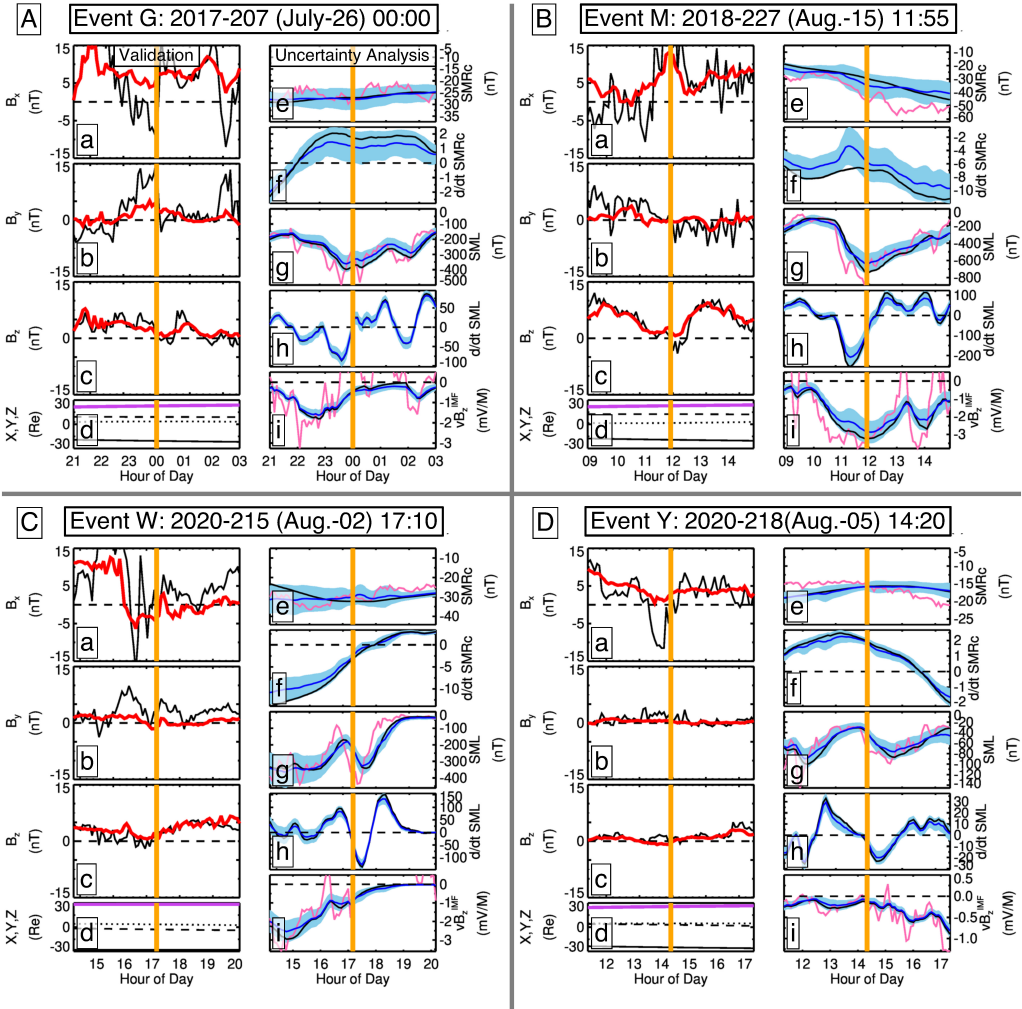


**Figure 5.** Validation and uncertainty analysis for events G, M, W, and Y, labeled (A)–(D) respectively. (a)–(c) The observed MMS4 5-min averaged GSM magnetic field components (black lines) and their DM reconstructions (red lines). (d) MMS ephemeris (in GSM) X (solid line), Y (dashed line), Z (dash-dotted line) and the radial distance (pink line). (e)–(i) The storm/substorm state binning parameters  $\langle SMRc \rangle$ ,  $D/\langle SMRc \rangle/Dt$ ,  $\langle SML \rangle$ ,  $D\langle SML \rangle/Dt$ , and  $\langle vB_s^{IMF} \rangle$  as described in section 2.2, shown by black lines as compared to their means over the NNs (blue lines). The light blue shading shows the standard deviations  $\pm 1\sigma$  of the NNs. Pink lines in Figs. 4E, 4G, and 4I show the original 5-min OMNI data for the parameters  $SMRc$  (pressure-corrected  $SMR$  (Tsyganenko, Andreeva, Sitnov, et al., 2021)),  $SML$ , and  $vB_s^{IMF}$ . Yellow vertical lines indicate the moment of the spatial reconstructions shown in Figs. 1, 2, and 3.

607 is marked by the formation of a new X-line  $\approx 24R_E$  from the Earth, which fades away later in  
 608 the recovery phase (Figure 6f). This evolution picture is consistent the original description of the  
 609 substorm cycle (Hones Jr., 1984; Baker et al., 1996).

610 Note that this is not the only X-line in this global picture, as the reconstructions also show  
 611 the persistent presence of a more distant X-line beyond  $\approx 24R_E$  distance (e.g., at  $r \approx 28R_E$  in  
 612 Figure 6e). In contrast to the widespread prejudice that magnetic reconnection only occurs with  
 613 the onset of a substorm, the existence of such a pre-onset X-line was conjectured already in the  
 614 seminal paper by Hones Jr. (1984). Moreover, without the formation of such an X-line and a rel-  
 615 atively steady reconnection there it is difficult to explain observations of the lobe magnetic flux  
 616 saturation in the last 40 minutes for a significant fraction of substorm growth phases (Shukhtina  
 617 et al., 2014). Two X-lines with relatively steady (around  $30R_E$ ) and unsteady (around  $20R_E$ ) re-  
 618 connection regimes were resolved using the DM approach by Sitnov et al. (2021) who explic-  
 619 itly evaluated the steadiness of reconnection by investigating the meridional distributions of the  
 620 in-plane ( $B_x$  and  $B_z$ ) components of the magnetic field before and after onset and invoking the  
 621 Faraday's law  $\partial E_y / \partial x = -\partial B_z / \partial t, \partial E_y / \partial z = \partial B_x / \partial t$ . They also compared the results with 3D  
 622 PIC simulations of the tail equilibria that revealed similar X-lines with steady and unsteady re-  
 623 connection.

624 The general misconception that the change of magnetic topology always results in explo-  
 625 sive reconnection is at variance with the large family of self-consistent X-line plasma equilib-  
 626 ria (e.g., Yoon & Lui, 2005, and refs. therein). Their PIC simulations reveal both active recon-  
 627 nection regimes (Sitnov & Swisdak, 2011) and steady configurations (Sitnov et al., 2013). Af-  
 628 ter all, stagnant plasmoids are known in observations (e.g., Nishida et al., 1986). It is also worth  
 629 noting here that the statistics of bursty bulk flows (Juusola et al., 2011) suggests that X-lines (and  
 630 the corresponding fast flows) can appear in any phases of substorms.

631 Other substorms associated with events C/D, M, and U show similar "classic substorm" 632 signatures with the new X-lines arising at the onset and fading away at the end of the recovery 633 phase. In cases of weaker substorms (events C and D with  $\min(SML) > -400$  nT), the new X- 634 lines are less pronounced (Figures S2). In case of storm-time substorms (event M), the  $B_z$  vari- 635 ations, and especially dipolarization effects are much stronger (Figure 2b). At the same time, new 636 X-lines may form closer to the Earth ( $\sim 15R_E$ ) consistent with in-situ observations (Angelopoulos 637 et al., 2020).

638 As an example of relatively unusual substorm activity associated with the reconstructed 639 X-lines we consider the tail evolution around event Y that occurred on 5 August 2020 at 14:20 UT. 640 According to Figure 7e (red line), during this event the reconstructed  $B_z$  component becomes neg- 641 ative at 13:15 UT and continues to be negative through 14:20 UT. Event Y corresponds to a marked 642 reduction of the  $SML$  index (Figure 5Dg). Therefore, at first sight, magnetic reconnection starts 643 well before the substorm onset, even before the beginning of the growth phase of this substorm. 644 This inconsistency (the gap between the red and black lines in Figure 7e) appears to be confirmed 645 by MMS4 observations, which show positive  $B_z$  during the interval 13:35–14:10 UT (black line) 646 in contrast to a negative  $B_z$  in the DM reconstructions (red line). MMS observations also sug- 647 gest that the plasma sheet was quiet during that period (Figure 7a).

648 However, closer examination shows a more complex picture with far better consistency be- 649 tween the DM reconstructions, ground-based data, and in-situ observations. First, according to 650 Figure 5Dg, the reconstructed  $B_z$  becomes negative in the midst of the recovery phase of a ear- 651 lier substorm ( $\sim 13:00$  UT), with a persistent solar wind input  $vB_z < 0$  for about two hours prior 652 to event Y (Figure 5Di).

653 Second, according to Figures 7b–e, during the last 30 minutes before event Y (13:40–14:10 654 UT) MMS was outside the plasma sheet with  $|B_x| \sim 10$  nT and a plasma  $\beta$  generally less than 655 unity. Moreover, the positive  $B_z$  profile correlated with  $B_x$  and  $B_y$  enhancements suggesting that 656 the current sheet was bent or flapping and that the observed positive  $B_z$  was a consequence. In 657 any case, the measured positive  $B_z$  was not observed while MMS was in the plasma sheet. Fur-

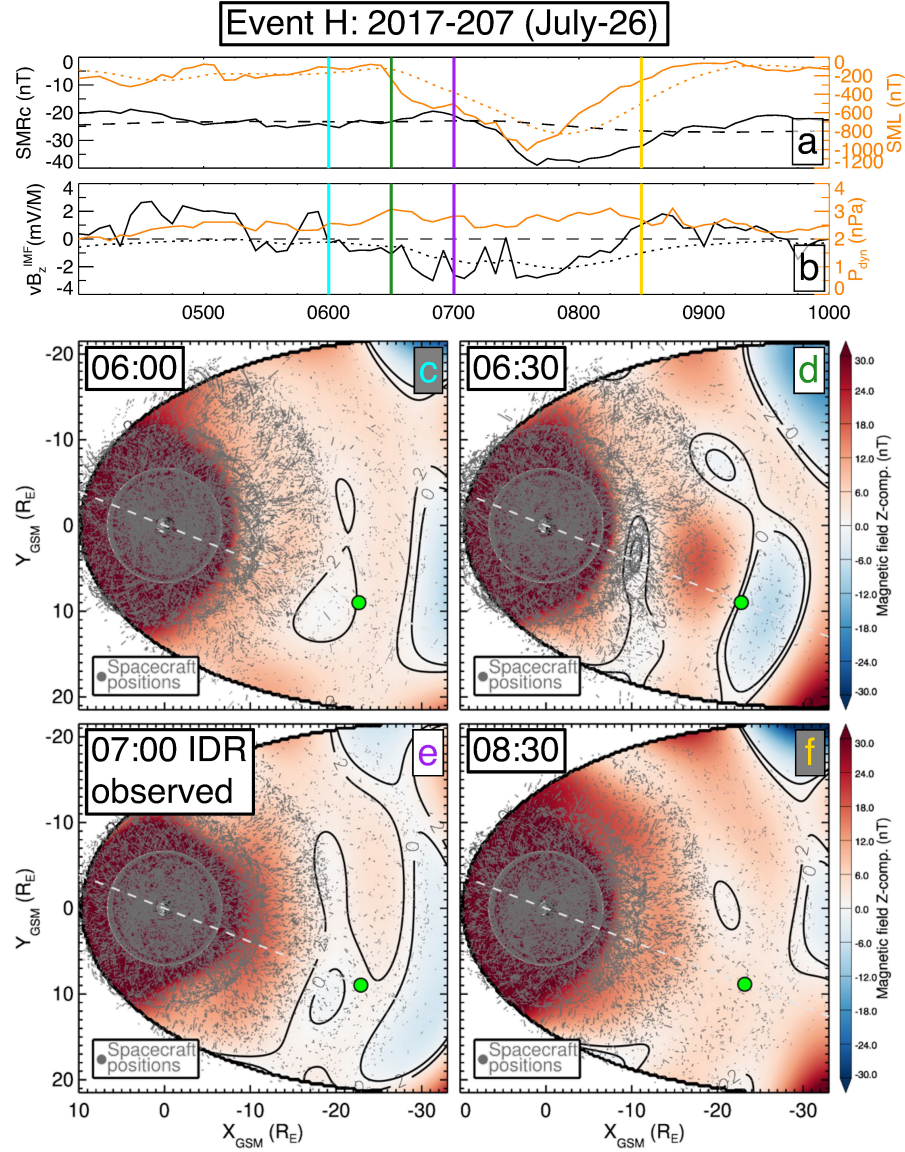


**Figure 6.** Evolution of X-lines during the 26 July 2017 substorm containing event H (panel e). (a and b) Geomagnetic indices and solar wind parameters in a format as shown previously. (c)–(f) Equatorial magnetic field,  $B_z$ , snapshots in a similar format as Figure 2 for four different times during the 26 July 2017 substorm. The four times are indicated in panels (a) and (b) by the vertical lines.

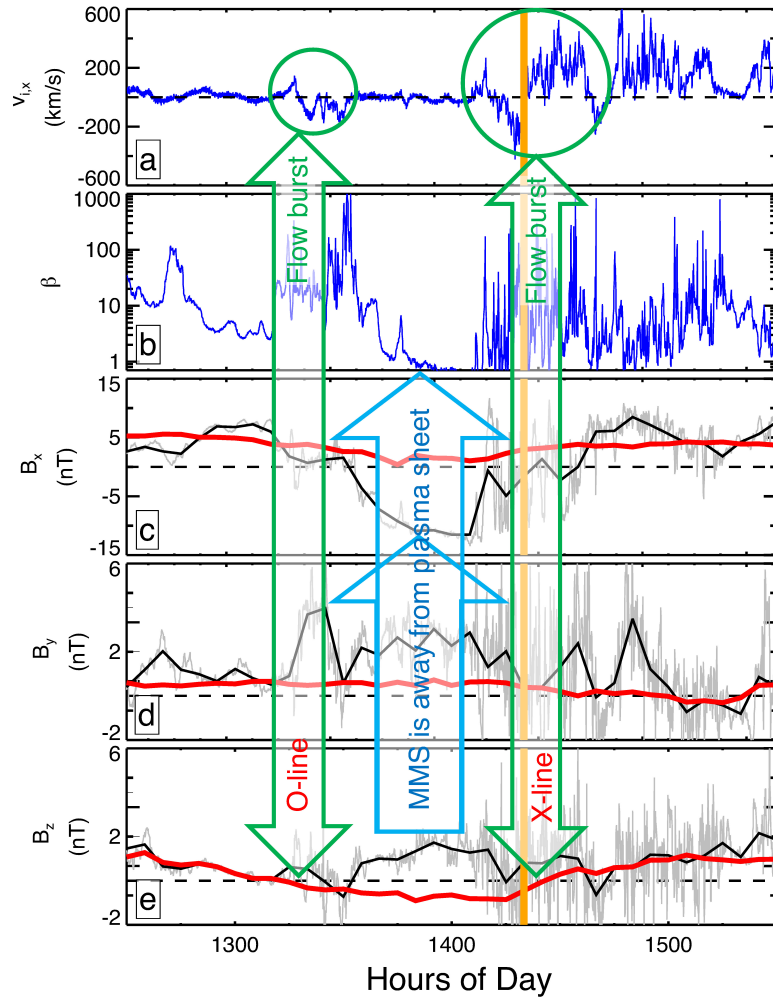


**Figure 7.** Unusual substorm activity around event Y. (a) the ion bulk flow velocity,  $v_{i,x}$ . (b) plasma beta computed from measurements of ions. (c–e) The observed MMS4 5-min averaged GSM magnetic field components (black lines) and their DM reconstructions (red lines) similar to Figure 5Da–5Dc but with different ranges. Light grey lines show the magnetic field components before the averaging.

thermore, during the earlier period (13:15–13:30 UT), when MMS was indeed inside the plasma sheet, it did observe significant tailward plasma flows, consistent with our reconstruction of another  $B_z = 0$  crossing (O-line) around 13:15 UT (Figure 7a). In other words, prior to event Y, the plasma sheet was active and its activity matched our reconstructed magnetic field. Before 13:00 there was no inconsistency between our reconstructions and MMS observations at all (the error is less than 1 nT). Thus, our magnetic field reconstruction is quite consistent with MMS data, both the magnetic field and plasma data.

## 6 Conclusions

The consistency of the DM picture of the 2017–2020 MMS IDR alphabet suggests that, in spite of the extreme paucity of in-situ observations, DM successfully reconstructs the overall structure of magnetotail X- and O-lines implying they are strongly self-organized on the global scale. It also supports Speiser proton orbits as the theoretical mechanism for the formation of an embedded thin current sheet in the magnetotail. The X-lines vary in length from 5 to  $40R_E$ , with the shorter ones tending to form inside of  $\sim 20R_E$  while the longer ones,  $\sim 40R_E$ , appear beyond  $25R_E$ . The concurrent appearance of such near-Earth and midtail X-lines is consistent with the original conjectures regarding new X-line formation during substorms (Hones Jr., 1984). It also explains the detection of X-lines as discrete points in radial distance in remote sensing (Angelopoulos et al., 2013, Fig. 3C) as well as the stepwise retreat of magnetic reconnection regions suggested by their auroral manifestations and confirmed by in-situ observations (Ieda et al., 2016). The persistent formation of X-lines near  $30R_E$  has also been confirmed by the statistical analysis of the travelling compression regions (Imber et al., 2011). The success of our X-line reconstruction indicates that year after year, the spatial/temporal patterns of storms and substorms in the Earth's magnetotail are highly recurrent and hence reproducible with historic data, while magnetic reconnection controls the global state of the magnetosphere reflected in its activity indices, their trends, and the solar wind energy input.

## 683 Data Availability Statement

The data used in the paper are archived on Zenodo (Stephens et al., 2022). For each of the 26 IDR events, files are included that detail: time intervals identified using the nearest-neighbor search and the resulting subset of magnetometer data and their associated weights, files containing the fit set of coefficients and parameters for the model, and the digital model output data that were used in constructing the figures. The compiled magnetometer database used in this study is available on the SPDF website (Korth et al., 2018). This study extended this database with the addition of MMS magnetometer data which has also been included in the Zenodo archive. The SMR and SML indices obtained from the SuperMAG web page are also included in the Zenodo archive. The data describing the solar wind conditions were taken from the 5-min OMNI data (Papitashvili & King, 2020).

## 694 Acknowledgments

The authors acknowledge useful discussions with G. Clark, R. Nakamura, S. Sharma, H. Spence, V. Titov, J. Vandegriff, D. Vassiliadis, and J. Zhang. They thank the SuperMag team and their collaborators, which provided the global indices of the storm and substorm activity. They also thank the teams who created and provided Geotail, Polar, IMP 8, Cluster, THEMIS, Van Allen Probes, MMS and GOES data obtained via NSSDC CDAWeb online facility, as well as Wind and ACE solar wind/IMF data that went into the production of the OMNI data obtained via NASA/GSFC's Space Physics Data Facility's OMNIWeb service. This work was funded by NASA grants 80NSSC19K0074, 80NSSC20K1271, 80NSSC20K1787, as well as NSF grants AGS-1702147 and AGS-1744269. N. A. Tsyganenko acknowledges support of the RFBR grant 20-05-00218. The work on this paper for MIS and GKS also benefited greatly from the discussions at the ISSI workshops, "Magnetotail Dipolarizations: Archimedes Force or Ideal Collapse?" and "Imaging the invisible: Unveiling the global structure of Earth's dynamic magnetosphere", held in May 2022.

707 **References**

708 Alken, P., Thébault, E., Beggan, C. D., Amit, H., Aubert, J., Baerenzung, J., ... Zhou,  
 709 B. (2021, December). International geomagnetic reference field: the thirteenth  
 710 generation. *Earth, Planets and Space*, 73(1), 49. doi: <https://doi.org/10.1186/s40623-020-01288-x>

712 Angelopoulos, V., Artemyev, A., Phan, T. D., & Miyashita, Y. (2020, January). Near-Earth  
 713 magnetotail reconnection powers space storms. *Nature Physics*, 16(3), 317-321. doi:  
 714 <https://doi.org/10.1038/s41567-019-0749-4>

715 Angelopoulos, V., McFadden, J. P., Larson, D., Carlson, C. W., Mende, S. B., Frey, H., ...  
 716 Kepko, L. (2008). Tail reconnection triggering substorm onset. *Science*, 321(5891),  
 717 931-935. Retrieved from <https://science.sciencemag.org/content/321/5891/931> doi: <https://doi.org/10.1126/science.1160495>

719 Angelopoulos, V., Runov, A., Zhou, X.-Z., Turner, D. L., Kiehas, S. A., Li, S.-S., & Shino-  
 720 hara, I. (2013). Electromagnetic energy conversion at reconnection fronts. *Science*,  
 721 341(6153), 1478-1482. Retrieved from <https://science.sciencemag.org/content/341/6153/1478> doi: <https://doi.org/10.1126/science.1236992>

723 Baker, D. N., Pulkkinen, T. I., Angelopoulos, V., Baumjohann, W., & McPherron, R. L.  
 724 (1996). Neutral line model of substorms: Past results and present view. *Journal of Geophysical Research: Space Physics*, 101(A6), 12975-13010. doi:  
 725 <https://doi.org/10.1029/95JA03753>

727 Birn, J., Hesse, M., & Schindler, K. (1996). Mhd simulations of magnetotail dynamics. *Journal of Geophysical Research: Space Physics*, 101(A6), 12939-12954. doi: <https://doi.org/10.1029/96JA00611>

730 Borovsky, J. E., & Yakymenko, K. (2017). Substorm occurrence rates, substorm recurrence  
 731 times, and solar wind structure. *Journal of Geophysical Research: Space Physics*,  
 732 122(3), 2973-2998. doi: <https://doi.org/10.1002/2016JA023625>

733 Burch, J. L., Moore, T. E., Torbert, R. B., & Giles, B. L. (2016, March). Magnetospheric  
 734 Multiscale Overview and Science Objectives. *Space Science Reviews*, 199(1-4), 5-21.  
 735 doi: <https://doi.org/10.1007/s11214-015-0164-9>

736 Burch, J. L., Torbert, R. B., Phan, T. D., Chen, L.-J., Moore, T. E., Ergun, R. E., ...  
 737 Chandler, M. (2016). Electron-scale measurements of magnetic reconnection in space.  
 738 *Science*, 352(6290), 10.1126/science.aaf2939. Retrieved from  
 739 <https://science.sciencemag.org/content/352/6290/aaf2939> doi:  
 740 <https://doi.org/10.1126/science.aaf2939>

741 Burton, R. K., McPherron, R. L., & Russell, C. T. (1975). An empirical relationship between  
 742 interplanetary conditions and dst. *Journal of Geophysical Research (1896-1977)*,  
 743 80(31), 4204-4214. doi: <https://doi.org/10.1029/JA080i031p04204>

744 Camporeale, E. (2019). The challenge of machine learning in space weather: Nowcast-  
 745 ing and forecasting. *Space Weather*, 17(8), 1166-1207. doi: <https://doi.org/10.1029/2018SW002061>

747 Chen, L.-J., Wang, S., Hesse, M., Ergun, R. E., Moore, T., Giles, B., ... Lindqvist,  
 748 P.-A. (2019). Electron diffusion regions in magnetotail reconnection under  
 749 varying guide fields. *Geophysical Research Letters*, 46(12), 6230-6238. doi:  
 750 <https://doi.org/10.1029/2019GL082393>

751 Childs, H., Brugger, E., Whitlock, B., Meredith, J., Ahern, S., Pugmire, D., ... Navrátil,  
 752 P. (2012, October). Visit: An end-user tool for visualizing and analyzing very large  
 753 data. In *High performance visualization-enabling extreme-scale scientific insight*  
 754 (p. 357-372). doi: <https://doi.org/10.1201/b12985>

755 Cowley, S. (1981). Magnetospheric asymmetries associated with the y-component of the  
 756 IMF. *Planetary and Space Science*, 29(1), 79-96. Retrieved from <https://www.sciencedirect.com/science/article/pii/0032063381901410> doi: [https://doi.org/10.1016/0032-0633\(81\)90141-0](https://doi.org/10.1016/0032-0633(81)90141-0)

759 Dungey, J. W. (1961). Interplanetary magnetic field and the auroral zones. *Phys. Rev. Lett.*,  
 760 6, 47-48. Retrieved from <https://link.aps.org/doi/10.1103/PhysRevLett.6.47> doi: <https://doi.org/10.1103/PhysRevLett.6.47>

762 Eastwood, J. P., Phan, T. D., Øieroset, M., & Shay, M. A. (2010). Average properties of  
 763 the magnetic reconnection ion diffusion region in the earth's magnetotail: The 2001-  
 764 2005 Cluster observations and comparison with simulations. *Journal of Geophysical  
 765 Research: Space Physics*, 115(A8), <https://doi.org/10.1029/2009JA014962>. doi:  
 766 <https://doi.org/10.1029/2009JA014962>

767 Farrugia, C. J., Rogers, A. J., Torbert, R. B., Genestreti, K. J., Nakamura, T. K. M., Lavraud,  
 768 B., ... Dors, I. (2021). An encounter with the ion and electron diffusion regions at  
 769 a flapping and twisted tail current sheet. *Journal of Geophysical Research: Space  
 770 Physics*, 126(3), e2020JA028903. doi: <https://doi.org/10.1029/2020JA028903>

771 Fuselier, S. A., Trattner, K. J., & Petrinec, S. M. (2011). Antiparallel and component re-  
 772 connection at the dayside magnetopause. *Journal of Geophysical Research: Space  
 773 Physics*, 116(A10), <https://doi.org/10.1029/2011JA016888>. Retrieved from <https://agupubs.onlinelibrary.wiley.com/doi/abs/10.1029/2011JA016888> doi:  
 774 <https://doi.org/10.1029/2011JA016888>

775 Gjerloev, J. W. (2012). The supermag data processing technique. *Journal of Geophysical Re-  
 776 search: Space Physics*, 117(A9), <https://doi.org/10.1029/2012JA017683>. doi: <https://doi.org/10.1029/2012JA017683>

777 Gonzalez, W. D., Joselyn, J. A., Kamide, Y., Kroehl, H. W., Rostoker, G., Tsurutani,  
 778 B. T., & Vasylunas, V. M. (1994). What is a geomagnetic storm? *Journal  
 779 of Geophysical Research: Space Physics*, 99(A4), 5771-5792. Retrieved from  
 780 <https://agupubs.onlinelibrary.wiley.com/doi/abs/10.1029/93JA02867>  
 781 doi: <https://doi.org/10.1029/93JA02867>

782 Greene, J. M. (1988). Geometrical properties of three-dimensional reconnecting mag-  
 783 netic fields with nulls. *Journal of Geophysical Research: Space Physics*, 93(A8),  
 784 8583-8590. doi: <https://doi.org/10.1029/JA093iA08p08583>

785 Griton, L., Pantellini, F., & Meliani, Z. (2018). Three-dimensional magnetohydrody-  
 786 namic simulations of the solar wind interaction with a hyperfast-rotating uranus.  
 787 *Journal of Geophysical Research: Space Physics*, 123(7), 5394-5406. doi:  
 788 <https://doi.org/10.1029/2018JA025331>

789 Hones Jr., E. W. (1984). Plasma sheet behavior during substorms. In *Magnetic recon-  
 790 nection in space and laboratory plasmas* (p. 178-184). American Geophysical Union  
 791 (AGU). Retrieved from <https://agupubs.onlinelibrary.wiley.com/doi/abs/10.1029/GM030p0178> doi: <https://doi.org/10.1029/GM030p0178>

792 Ieda, A., Nishimura, Y., Miyashita, Y., Angelopoulos, V., Runov, A., Nagai, T., ... Machida,  
 793 S. (2016). Stepwise tailward retreat of magnetic reconnection: Themis observations  
 794 of an auroral substorm. *Journal of Geophysical Research: Space Physics*, 121(5),  
 795 4548-4568. doi: <https://doi.org/10.1002/2015JA022244>

796 Imber, S. M., Slavin, J. A., Auster, H. U., & Angelopoulos, V. (2011). A themis sur-  
 797 vey of flux ropes and traveling compression regions: Location of the near-earth re-  
 798 connection site during solar minimum. *Journal of Geophysical Research: Space  
 799 Physics*, 116(A2), <https://doi.org/10.1029/2010JA016026>. doi: <https://doi.org/10.1029/2010JA016026>

800 Jackson, D. D. (1972, 06). Interpretation of Inaccurate, Insufficient and Incon-  
 801 sistent Data. *Geophysical Journal International*, 28(2), 97-109. Retrieved  
 802 from <https://doi.org/10.1111/j.1365-246X.1972.tb06115.x> doi:  
 803 <https://doi.org/10.1111/j.1365-246X.1972.tb06115.x>

804 Ji, H., Daughton, W., Jara-Almonte, J., Le, A., Stanier, A., & Yoo, J. (2022). Magnetic re-  
 805 connection in the era of exascale computing and multiscale experiments. *Nature Re-  
 806 views Physics*, 4, 263-282. doi: <https://doi.org/10.1038/s42254-021-00419-x>

807 Juusola, L., Østgaard, N., Tanskanen, E., Partamies, N., & Snekvik, K. (2011). Earth-  
 808 ward plasma sheet flows during substorm phases. *Journal of Geophysical Research:  
 809 Space Physics*, 116(A10). Retrieved from <https://agupubs.onlinelibrary.wiley.com/doi/abs/10.1029/2011JA016852> doi: <https://doi.org/10.1029/2011JA016852>

810 Korth, H., Sitnov, M. I., & Stephens, G. K. (2018). *Magnetic field modeling database de-*

817 *scription final* [dataset]. NASA Space Physics Data Facility. Retrieved from [https://spdf.gsfc.nasa.gov/pub/data/aaa\\_special-purpose-datasets/empirical-magnetic-field-modeling-database-with-TS07D-coefficients/](https://spdf.gsfc.nasa.gov/pub/data/aaa_special-purpose-datasets/empirical-magnetic-field-modeling-database-with-TS07D-coefficients/)

818 Liemohn, M. W., McCollough, J. P., Jordanova, V. K., Ngwira, C. M., Morley, S. K.,  
 819 Cid, C., ... Vasile, R. (2018). Model evaluation guidelines for geomagnetic in-  
 820 dex predictions. *Space Weather*, 16(12), 2079-2102. Retrieved from <https://agupubs.onlinelibrary.wiley.com/doi/abs/10.1029/2018SW002067> doi:  
 821 <https://doi.org/10.1029/2018SW002067>

822 Liu, R., Kliem, B., Titov, V. S., Chen, J., Wang, Y., Wang, H., ... Wiegmann, T. (2016,  
 823 feb). STRUCTURE, STABILITY, AND EVOLUTION OF MAGNETIC FLUX  
 824 ROPES FROM THE PERSPECTIVE OF MAGNETIC TWIST. *The Astrophysical  
 825 Journal*, 818(2), 148. Retrieved from <https://doi.org/10.3847/0004-637x/818/2/148> doi: <https://doi.org/10.3847/0004-637x/818/2/148>

826 McPherron, R. L., Russell, C. T., & Aubry, M. P. (1973). Satellite studies of magnetospheric  
 827 substorms on august 15, 1968: 9. phenomenological model for substorms. *Journal of  
 828 Geophysical Research*, 78(16), 3131-3149.

829 Mead, G. D., & Beard, D. B. (1964). Shape of the geomagnetic field solar wind bound-  
 830 ary. *Journal of Geophysical Research (1896-1977)*, 69(7), 1169-1179. Retrieved  
 831 from <https://agupubs.onlinelibrary.wiley.com/doi/abs/10.1029/JZ069i007p01169> doi: <https://doi.org/10.1029/JZ069i007p01169>

832 Nagai, T., Fujimoto, M., Nakamura, R., Baumjohann, W., Ieda, A., Shinohara, I., ... Mukai,  
 833 T. (2005). Solar wind control of the radial distance of the magnetic reconne-  
 834 ction site in the magnetotail. *Journal of Geophysical Research: Space Physics*,  
 835 110(A9), <https://doi.org/10.1029/2005JA011207>. Retrieved from <https://agupubs.onlinelibrary.wiley.com/doi/abs/10.1029/2005JA011207> doi:  
 836 <https://doi.org/10.1029/2005JA011207>

837 Nagai, T., & Shinohara, I. (2022). Solar wind energy input: The primary control factor  
 838 of magnetotail reconnection site. *Journal of Geophysical Research: Space Physics*,  
 839 127(8), e2022JA030653. Retrieved from <https://agupubs.onlinelibrary.wiley.com/doi/abs/10.1029/2022JA030653> (e2022JA030653 2022JA030653)  
 840 doi: <https://doi.org/10.1029/2022JA030653>

841 Nelder, J. A., & Mead, R. (1965, 01). A Simplex Method for Function Minimization. *The  
 842 Computer Journal*, 7(4), 308-313. Retrieved from <https://doi.org/10.1093/comjnl/7.4.308> doi: <https://doi.org/10.1093/comjnl/7.4.308>

843 Newell, P. T., & Gjerloev, J. W. (2011). Evaluation of supermag auroral electrojet indices  
 844 as indicators of substorms and auroral power. *Journal of Geophysical Research: Space  
 845 Physics*, 116(A12), <https://doi.org/10.1029/2011JA016779>. Retrieved from <https://agupubs.onlinelibrary.wiley.com/doi/abs/10.1029/2011JA016779> doi:  
 846 <https://doi.org/10.1029/2011JA016779>

847 Newell, P. T., & Gjerloev, J. W. (2012). Supermag-based partial ring cur-  
 848 rent indices. *Journal of Geophysical Research: Space Physics*, 117(A5),  
 849 <https://doi.org/10.1029/2012JA017586>. Retrieved from <https://agupubs.onlinelibrary.wiley.com/doi/abs/10.1029/2012JA017586> doi:  
 850 <https://doi.org/10.1029/2012JA017586>

851 Nishida, A., Scholer, M., Terasawa, T., Bame, S. J., Gloeckler, G., Smith, E. J., & Zwickl,  
 852 R. D. (1986). Quasi-stagnant plasmoid in the middle tail: A new preexpansion  
 853 phase phenomenon. *Journal of Geophysical Research: Space Physics*, 91(A4), 4245-  
 854 4255. Retrieved from <https://agupubs.onlinelibrary.wiley.com/doi/abs/10.1029/JA091iA04p04245> doi: <https://doi.org/10.1029/JA091iA04p04245>

855 Papitashvili, N. E., & King, J. H. (2020). *Omni 5-min data* [dataset]. NASA Space Physics  
 856 Data Facility. Retrieved from <https://www.unavco.org/data/doi/10.7283/633E-1497> doi: [10.48322/gbpg-5r77](https://doi.org/10.48322/gbpg-5r77)

857 Partamies, N., Juusola, L., Tanskanen, E., & Kauristie, K. (2013). Statistical properties of  
 858 substorms during different storm and solar cycle phases. *Annales Geophysicae*, 31(2),  
 859 349-358. Retrieved from <https://www.ann-geophys.net/31/349/2013/> doi:  
 860 <https://doi.org/10.5194/angeo-31-349-2013>

872 <https://doi.org/10.5194/angeo-31-349-2013>

873 Phan, T. D., Eastwood, J. P., Shay, M. A., Drake, J. F., Sonnerup, B. U. Ö., Fujimoto,  
874 M., ... Magnes, W. (2018, May 01). Electron magnetic reconnection without  
875 ion coupling in Earth's turbulent magnetosheath. *Nature*, 557(7704), 202-  
876 206. Retrieved from <https://doi.org/10.1038/s41586-018-0091-5> doi:  
877 <https://doi.org/10.1038/s41586-018-0091-5>

878 Press, W. H., Teukolsky, S. A., Flannery, B. P., & Vetterling, W. T. (1992). *Numerical  
879 recipes in fortran: The art of scientific computing* (2nd ed.). USA: Cambridge University  
880 Press.

881 Reyes, P. I., Pinto, V. A., & Moya, P. S. (2021). Geomagnetic storm occurrence and their re-  
882 lation with solar cycle phases. *Space Weather*, 19(9), e2021SW002766. doi: <https://doi.org/10.1029/2021SW002766>

883 Rogers, A. J., Farrugia, C. J., & Torbert, R. B. (2019). Numerical algorithm for detecting  
884 ion diffusion regions in the geomagnetic tail with applications to mms tail season 1  
885 may to 30 september 2017. *Journal of Geophysical Research: Space Physics*, 124(8),  
886 6487-6503. Retrieved from <https://agupubs.onlinelibrary.wiley.com/doi/abs/10.1029/2018JA026429> doi: <https://doi.org/10.1029/2018JA026429>

887 Rogers, A. J., Farrugia, C. J., Torbert, R. B., & Rogers, T. J. (2021). Applying magnetic  
888 curvature to to MMS data to identify thin current sheets relative to tail reconne-  
889 ction. *Earth and Space Science Open Archive*, 12. doi: <https://doi.org/10.1002/essoar.10509282.1>

890 Runov, A., Sergeev, V. A., Baumjohann, W., Nakamura, R., Apatenkov, S., Asano, Y.,  
891 ... Rème, H. (2005). Electric current and magnetic field geometry in flapping  
892 magnetotail current sheets. *Annales Geophysicae*, 23(4), 1391-1403. Retrieved  
893 from <https://angeo.copernicus.org/articles/23/1391/2005/> doi:  
894 [10.5194/angeo-23-1391-2005](https://doi.org/10.5194/angeo-23-1391-2005)

895 Russell, C. T., & McPherron, R. L. (1973, Nov 01). The magnetotail and substorms. *Space  
896 Science Reviews*, 15(2), 205-266. Retrieved from <https://doi.org/10.1007/BF00169321> doi: 10.1007/BF00169321

897 Sergeev, V. A., Angelopoulos, V., Kubyshkina, M., Donovan, E., Zhou, X.-Z., Runov,  
898 A., ... Nakamura, R. (2011). Substorm growth and expansion onset as ob-  
899 served with ideal ground-spacecraft themis coverage. *Journal of Geophysical  
900 Research: Space Physics*, 116(A5), <https://doi.org/10.1029/2010JA015689>. doi:  
901 <https://doi.org/10.1029/2010JA015689>

902 Sergeev, V. A., Sormakov, D. A., Apatenkov, S. V., Baumjohann, W., Nakamura, R.,  
903 Runov, A. V., ... Nagai, T. (2006). Survey of large-amplitude flapping motions  
904 in the midtail current sheet. *Annales Geophysicae*, 24(7), 2015-2024. Retrieved  
905 from <https://angeo.copernicus.org/articles/24/2015/2006/> doi:  
906 [10.5194/angeo-24-2015-2006](https://doi.org/10.5194/angeo-24-2015-2006)

907 Shiota, D., Isobe, H., Chen, P. F., Yamamoto, T. T., Sakajiri, T., & Shibata, K. (2005, nov).  
908 Self-consistent magnetohydrodynamic modeling of a coronal mass ejection, coronal  
909 dimming, and a giant cusp-shaped arcade formation. *The Astrophysical Journal*,  
910 634(1), 663-678. Retrieved from <https://doi.org/10.1086/496943> doi:  
911 <https://doi.org/10.1086/496943>

912 Shue, J.-H., Song, P., Russell, C. T., Steinberg, J. T., Chao, J. K., Zastenker, G., ...  
913 Kawano, H. (1998). Magnetopause location under extreme solar wind conditions.  
914 *Journal of Geophysical Research: Space Physics*, 103(A8), 17691-17700. doi:  
915 <https://doi.org/10.1029/98JA01103>

916 Shukhtina, M. A., Dmitrieva, N. P., & Sergeev, V. A. (2014). On the conditions preced-  
917 ing sudden magnetotail magnetic flux unloading. *Geophysical Research Letters*, 41(4),  
918 1093-1099. Retrieved from <https://agupubs.onlinelibrary.wiley.com/doi/abs/10.1002/2014GL059290> doi: <https://doi.org/10.1002/2014GL059290>

919 Sibeck, D. G., Lopez, R. E., & Roelof, E. C. (1991). Solar wind control of the magnetopause  
920 shape, location, and motion. *Journal of Geophysical Research: Space Physics*, 96(A4),  
921 5489-5495. Retrieved from <https://agupubs.onlinelibrary.wiley.com/doi/>

abs/10.1029/90JA02464 doi: <https://doi.org/10.1029/90JA02464>

Sitnov, M. I., Birn, J., Ferdousi, B., Gordeev, E., Khotyaintsev, Y., Merkin, V., ... Zhou, X. (2019, June). Explosive Magnetotail Activity. *Space Science Reviews*, 215(4), 31. doi: <https://doi.org/10.1007/s11214-019-0599-5>

Sitnov, M. I., Buzulukova, N., Swisdak, M., Merkin, V. G., & Moore, T. E. (2013). Spontaneous formation of dipolarization fronts and reconnection onset in the magnetotail. *Geophysical Research Letters*, 40(1), 22-27. Retrieved from <https://agupubs.onlinelibrary.wiley.com/doi/abs/10.1029/2012GL054701> doi: <https://doi.org/10.1029/2012GL054701>

Sitnov, M. I., & Merkin, V. G. (2016). Generalized magnetotail equilibria: Effects of the dipole field, thin current sheets, and magnetic flux accumulation. *Journal of Geophysical Research: Space Physics*, 121(8), 7664-7683. Retrieved from <http://dx.doi.org/10.1002/2016JA023001> doi: 10.1002/2016JA023001

Sitnov, M. I., & Schindler, K. (2010). Tearing stability of a multiscale magnetotail current sheet. *Geophysical Research Letters*, 37(8). Retrieved from <https://agupubs.onlinelibrary.wiley.com/doi/abs/10.1029/2010GL042961> doi: <https://doi.org/10.1029/2010GL042961>

Sitnov, M. I., Sharma, A. S., Papadopoulos, K., & Vassiliadis, D. (2001, Dec). Modeling substorm dynamics of the magnetosphere: From self-organization and self-organized criticality to nonequilibrium phase transitions. *Phys. Rev. E*, 65, 016116. Retrieved from <https://link.aps.org/doi/10.1103/PhysRevE.65.016116> doi: <https://doi.org/10.1103/PhysRevE.65.016116>

Sitnov, M. I., Stephens, G. K., Motoba, T., & Swisdak, M. (2021). Data mining reconstruction of magnetotail reconnection and implications for its first-principle modeling. *Frontiers in Physics*, 9. Retrieved from <https://www.frontiersin.org/articles/10.3389/fphy.2021.644884> doi: <https://doi.org/10.3389/fphy.2021.644884>

Sitnov, M. I., Stephens, G. K., Tsyganenko, N. A., Miyashita, Y., Merkin, V. G., Motoba, T., ... Genestreti, K. J. (2019). Signatures of nonideal plasma evolution during substorms obtained by mining multimission magnetometer data. *Journal of Geophysical Research: Space Physics*, 124(11), 8427-8456. doi: <https://doi.org/10.1029/2019JA027037>

Sitnov, M. I., Stephens, G. K., Tsyganenko, N. A., Ukhorskiy, A. Y., Wing, S., Korth, H., & Anderson, B. J. (2017). Spatial structure and asymmetries of magnetospheric currents inferred from high-resolution empirical geomagnetic field models. In *Dawn-dusk asymmetries in planetary plasma environments* (p. 199-212). American Geophysical Union (AGU). doi: <https://doi.org/10.1002/9781119216346.ch15>

Sitnov, M. I., & Swisdak, M. (2011). Onset of collisionless magnetic reconnection in two-dimensional current sheets and formation of dipolarization fronts. *Journal of Geophysical Research: Space Physics*, 116(A12). Retrieved from <https://agupubs.onlinelibrary.wiley.com/doi/abs/10.1029/2011JA016920> doi: <https://doi.org/10.1029/2011JA016920>

Sitnov, M. I., Swisdak, M., Guzdar, P. N., & Runov, A. (2006). Structure and dynamics of a new class of thin current sheets. *Journal of Geophysical Research: Space Physics*, 111(A8), <https://doi.org/10.1029/2005JA011517>. doi: <https://doi.org/10.1029/2005JA011517>

Sitnov, M. I., Tsyganenko, N. A., Ukhorskiy, A. Y., & Brandt, P. C. (2008). Dynamical data-based modeling of the storm-time geomagnetic field with enhanced spatial resolution. *Journal of Geophysical Research: Space Physics*, 113(A7), 10.1029/2007JA013003. doi: <https://doi.org/10.1029/2007JA013003>

Sitnov, M. I., Ukhorskiy, A. Y., & Stephens, G. K. (2012). Forecasting of global data-binning parameters for high-resolution empirical geomagnetic field models. *Space Weather*, 10(9), 10.1029/2012SW000783. doi: <https://doi.org/10.1029/2012SW000783>

Speiser, T. W. (1965). Particle trajectories in model current sheets: 1. analytical solutions. *Journal of Geophysical Research (1896-1977)*, 70(17), 4219-4226. doi: <https://doi.org/10.1029/JA070i017p04219>

982 10.1029/JZ070i017p04219

983 Stephens, G. K., Bingham, S. T., Sitnov, M. I., Gkioulidou, M., Merkin, V. G., Korth, H.,  
 984 ... Ukhorskiy, A. Y. (2020). Storm time plasma pressure inferred from multimission  
 985 measurements and its validation using van allen probes particle data. *Space Weather*,  
 986 18(12), e2020SW002583. doi: <https://doi.org/10.1029/2020SW002583>

987 Stephens, G. K., & Sitnov, M. I. (2021). Concurrent empirical magnetic reconstruction of  
 988 storm and substorm spatial scales using data mining and virtual spacecraft. *Frontiers  
 989 in Physics*, 9, 210. Retrieved from <https://www.frontiersin.org/article/10.3389/fphy.2021.653111> doi: <https://doi.org/10.3389/fphy.2021.653111>

990 Stephens, G. K., Sitnov, M. I., Korth, H., Tsyganenko, N. A., Ohtani, S., Gkioulidou,  
 991 M., & Ukhorskiy, A. Y. (2019). Global empirical picture of magnetospheric  
 992 substorms inferred from multimission magnetometer data. *Journal of Geophysical  
 993 Research: Space Physics*, 124(2), 1085-1110. Retrieved from <https://agupubs.onlinelibrary.wiley.com/doi/abs/10.1029/2018JA025843> doi:  
 994 <https://doi.org/10.1029/2018JA025843>

995 Stephens, G. K., Sitnov, M. I., Weigel, R., Turner, D., Tsyganenko, N., Rogers, A., ...  
 996 Slavin, J. (2022). *Global structure of magnetotail reconnection revealed by mining space magnetometer data* [dataset]. Zenodo. Retrieved from <https://doi.org/10.5281/zenodo.6862829> doi: 10.5281/zenodo.6862829

997 Tanaka, T., Ebihara, Y., Watanabe, M., Den, M., Fujita, S., Kikuchi, T., ... Kataoka, R.  
 998 (2021). Roles of the m-i coupling and plasma sheet dissipation on the growth-  
 999 phase thinning and subsequent transition to the onset. *Journal of Geophysical  
 1000 Research: Space Physics*, 126(12), e2021JA029925. Retrieved from <https://agupubs.onlinelibrary.wiley.com/doi/abs/10.1029/2021JA029925> doi:  
 1001 <https://doi.org/10.1029/2021JA029925>

1002 Torbert, R. B., Burch, J. L., Phan, T. D., Hesse, M., Argall, M. R., Shuster, J., ... Saito,  
 1003 Y. (2018). Electron-scale dynamics of the diffusion region during symmetric  
 1004 magnetic reconnection in space. *Science*, 362(6421), 1391-1395. Retrieved  
 1005 from <https://science.sciencemag.org/content/362/6421/1391> doi:  
 1006 <https://doi.org/10.1126/science.aat2998>

1007 Tsyganenko, N. A. (1991). Methods for quantitative modeling of the magnetic field from  
 1008 Birkeland currents. *Planetary and Space Science*, 39(4), 641 - 654. Retrieved from  
 1009 <http://www.sciencedirect.com/science/article/pii/003206339190058I>  
 1010 doi: [https://dx.doi.org/10.1016/0032-0633\(91\)90058-I](https://dx.doi.org/10.1016/0032-0633(91)90058-I)

1011 Tsyganenko, N. A. (1995). Modeling the earth's magnetospheric magnetic field confined  
 1012 within a realistic magnetopause. *Journal of Geophysical Research: Space Physics*,  
 1013 100(A4), 5599-5612. doi: <https://doi.org/10.1029/94JA03193>

1014 Tsyganenko, N. A. (1998). Modeling of twisted/warped magnetospheric config-  
 1015 urations using the general deformation method. *Journal of Geophysical Re-  
 1016 search: Space Physics*, 103(A10), 23551-23563. Retrieved from <https://agupubs.onlinelibrary.wiley.com/doi/abs/10.1029/98JA02292> doi:  
 1017 <https://doi.org/10.1029/98JA02292>

1018 Tsyganenko, N. A. (2002a). A model of the near magnetosphere with a dawn-dusk asym-  
 1019 metry 1. Mathematical structure. *Journal of Geophysical Research: Space Physics*,  
 1020 107(A8), SMP 12-1-SMP 12-15. doi: <https://doi.org/10.1029/2001JA000219>

1021 Tsyganenko, N. A. (2002b). A model of the near magnetosphere with a dawn-dusk asymme-  
 1022 try 2. parameterization and fitting to observations. *Journal of Geophysical Research:  
 1023 Space Physics*, 107(A8), SMP 10-1-SMP 10-17. Retrieved from <https://agupubs.onlinelibrary.wiley.com/doi/abs/10.1029/2001JA000220> doi: <https://doi.org/10.1029/2001JA000220>

1024 Tsyganenko, N. A. (2013). Data-based modelling of the earth's dynamic magnetosphere: a  
 1025 review. *Annales Geophysicae*, 31(10), 1745-1772. Retrieved from <https://angeo.copernicus.org/articles/31/1745/2013/> doi: <https://doi.org/10.5194/angeo-31-1745-2013>

1026 Tsyganenko, N. A. (2014). Data-based modeling of the geomagnetosphere with an imf-

1037 dependent magnetopause. *Journal of Geophysical Research: Space Physics*, 119(1),  
 1038 335-354. doi: <https://doi.org/10.1002/2013JA019346>

1039 Tsyganenko, N. A., Andreeva, V., Kubyshkina, M., Sitnov, M. I., & Stephens, G. K. (2021).  
 1040 Data-based modeling of the earth's magnetic field. In *Magnetospheres in the solar*  
 1041 *system* (p. 617-635). American Geophysical Union (AGU). Retrieved from <https://agupubs.onlinelibrary.wiley.com/doi/abs/10.1002/9781119815624.ch39>  
 1042 doi: <https://doi.org/10.1002/9781119815624.ch39>

1043 Tsyganenko, N. A., Andreeva, V. A., & Gordeev, E. I. (2015). Internally and ex-  
 1044 ternally induced deformations of the magnetospheric equatorial current as in-  
 1045 ferred from spacecraft data. *Annales Geophysicae*, 33(1), 1–11. Retrieved from  
 1046 <https://angeo.copernicus.org/articles/33/1/2015/> doi: <https://doi.org/10.5194/angeo-33-1-2015>

1047 Tsyganenko, N. A., Andreeva, V. A., Sitnov, M. I., Stephens, G. K., Gjerloev, J. W., Chu,  
 1048 X., & Troshichev, O. A. (2021). Reconstructing substorms via historical data min-  
 1049 ing: Is it really feasible? *Journal of Geophysical Research: Space Physics*, 126(10),  
 1050 e2021JA029604. doi: <https://doi.org/10.1029/2021JA029604>

1051 Tsyganenko, N. A., & Fairfield, D. H. (2004). Global shape of the magnetotail current  
 1052 sheet as derived from geotail and polar data. *Journal of Geophysical Research: Space*  
 1053 *Physics*, 109(A3), <https://doi.org/10.1029/2003JA010062>. doi: <https://doi.org/10.1029/2003JA010062>

1054 Tsyganenko, N. A., & Sitnov, M. I. (2005). Modeling the dynamics of the inner magne-  
 1055 tosphere during strong geomagnetic storms. *Journal of Geophysical Research: Space*  
 1056 *Physics*, 110(A3). doi: <https://doi.org/10.1029/2004JA010798>

1057 Tsyganenko, N. A., & Sitnov, M. I. (2007). Magnetospheric configurations from a high-  
 1058 resolution data-based magnetic field model. *Journal of Geophysical Research: Space*  
 1059 *Physics*, 112(A6), 10.1029/2007JA012260. doi: <https://doi.org/10.1029/2007JA012260>

1060 Vassiliadis, D. (2006). Systems theory for geospace plasma dynamics. *Reviews of Geo-*  
 1061 *physics*, 44(2), <https://doi.org/10.1029/2004RG000161>. doi: <https://doi.org/10.1029/2004RG000161>

1062 Vassiliadis, D., Klimas, A., & Baker, D. (1999). Models of dst geomagnetic ac-  
 1063 tivity and of its coupling to solar wind parameters. *Physics and Chemistry of*  
 1064 *the Earth, Part C: Solar, Terrestrial & Planetary Science*, 24(1), 107-112. Re-  
 1065 trived from <https://www.sciencedirect.com/science/article/pii/S1464191798000166> (International Symposium on Solar-Terrestrial Coupling  
 1066 Processes) doi: [https://doi.org/10.1016/S1464-1917\(98\)00016-6](https://doi.org/10.1016/S1464-1917(98)00016-6)

1067 Vassiliadis, D., Klimas, A. J., Baker, D. N., & Roberts, D. A. (1995). A description of the  
 1068 solar wind-magnetosphere coupling based on nonlinear filters. *Journal of Geophysical*  
 1069 *Research: Space Physics*, 100(A3), 3495-3512. Retrieved from <https://agupubs.onlinelibrary.wiley.com/doi/abs/10.1029/94JA02725> doi: <https://doi.org/10.1029/94JA02725>

1070 Verleysen, M., & François, D. (2005). The curse of dimensionality in data mining and time  
 1071 series prediction. In J. Cabestany, A. Prieto, & F. Sandoval (Eds.), *Computational in-*  
 1072 *telligence and bioinspired systems* (pp. 758–770). Berlin, Heidelberg: Springer Berlin  
 1073 Heidelberg.

1074 Wang, C.-P., Lyons, L. R., Nagai, T., & Samson, J. C. (2004). Midnight radial profiles of the  
 1075 quiet and growth-phase plasma sheet: The geotail observations. *Journal of Geophys-  
 1076 ical Research: Space Physics*, 109(A12), <https://doi.org/10.1029/2004JA010590>. doi:  
 1077 <https://doi.org/10.1029/2004JA010590>

1078 Wettschereck, D., Aha, D. W., & Mohri, T. (1997, Feb 01). A review and empirical evalua-  
 1079 tion of feature weighting methods for a class of lazy learning algorithms. *Artificial In-*  
 1080 *telligence Review*, 11(1), 273-314. Retrieved from <https://doi.org/10.1023/A:1006593614256> doi: 10.1023/A:1006593614256

1081 Williams, T., Shulman, S., Ottenstein, N., Palmer, E., Riley, C., Letourneau, S., ... Go-  
 1082 dine, D. (2020). Operational techniques for dealing with long eclipses during

1092 the mms extended mission. In *2020 ieee aerospace conference* (p. 1-12). doi:  
1093 <https://doi.org/10.1109/AERO47225.2020.9172276>

1094 Xiao, C. J., Wang, X. G., Pu, Z. Y., Zhao, H., Wang, J. X., Ma, Z. W., ... Escoubet, C. P.  
1095 (2006, Jul 01). In situ evidence for the structure of the magnetic null in a 3d reconnec-  
1096 tion event in the earth's magnetotail. *Nature Physics*, 2(7), 478-483. Retrieved from  
1097 <https://doi.org/10.1038/nphys342> doi: <https://doi.org/10.1038/nphys342>

1098 Yoon, P. H., & Lui, A. T. Y. (2005). A class of exact two-dimensional kinetic current  
1099 sheet equilibria. *Journal of Geophysical Research: Space Physics*, 110(A1). Re-  
1100 trieval from <https://agupubs.onlinelibrary.wiley.com/doi/abs/10.1029/2003JA010308> doi: <https://doi.org/10.1029/2003JA010308>

1101